Magnetosphere-ionosphere coupling at Jupiter: Effect of field-aligned potentials on angular momentum transport

L. C. Ray,[1] R. E. Ergun,[1] P. A. Delamere,[1] and F. Bagenal[1]

Received 3 March 2010; revised 26 April 2010; accepted 17 May 2010; published 17 September 2010.

[1] We present a time-independent model of Jupiter's rotation-driven aurora based on angular momentum conservation, including the effects of a field-aligned potential ($\Phi_{\parallel}$) and an ionospheric conductivity that is modified by precipitating electrons. We argue that $\Phi_{\parallel}$ arises from a limit to field-aligned current at high latitudes, and hence, we apply a current-voltage relation, which takes into account the low plasma densities at high latitudes. The resulting set of nonlinear equations that govern the behavior of angular momentum transfer is underconstrained and leads to a set of solutions, including those derived in earlier work. We show that solutions with high angular momentum transfer, large radial currents, and small mass transport rates ($\dot{M} \leq 1000$ kg/s) exist. Our set of solutions can reproduce many of the observed characteristics of Jupiter's main auroral oval, including the energy of the precipitating electrons, the energy flux into the ionosphere, the width of the aurora at the ionosphere, and net radial current across the field for a radial mass transport value of ~500 kg/s.

Citation: Ray, L. C., R. E. Ergun, P. A. Delamere, and F. Bagenal (2010), Magnetosphere-ionosphere coupling at Jupiter: Effect of field-aligned potentials on angular momentum transport, *J. Geophys. Res.*, *115*, A09211, doi:10.1029/2010JA015423.

1. Introduction

[2] Jupiter displays several types of auroral processes that include, from low to high latitudes, satellite-driven aurora (spots), rotation-driven aurora (the main oval), and a variable polar aurora which maps to the outer magnetosphere [*Clarke et al.*, 2004, 2009; *Nichols et al.*, 2009]. The main auroral oval is directly related to the transfer of angular momentum from Jupiter to its magnetosphere [*Hill*, 1979]. Iogenic plasma moves outward from Jupiter via a centrifugally driven interchange instability [*Krupp et al.*, 2004], which requires the transfer of angular momentum from Jupiter to keep the magnetospheric plasma near corotation. The angular momentum transfer is mediated by an upward current from Jupiter's ionosphere travelling along **B** to the equator and then radially outward to drive a magnetospheric $\mathbf{J} \times \mathbf{B}$ force, accelerating the plasma toward corotation (see Figure 1). However, between ~17 and ~20 Jovian radii (R_J) the azimuthal flow begins to depart from corotation [*McNutt et al.*, 1979; *Krupp et al.*, 2001; *Frank and Paterson*, 2002]. The main auroral oval is associated with this current system and ultimately the breakdown in corotation. Heretofore, the limiting factor in angular momentum transfer has been assumed to be the height-integrated Pedersen conductivity of Jupiter's ionosphere, Σ_P. In this paper we examine the effects of a high-latitude current-voltage relation and the resulting field-aligned potentials on angular momentum transfer.

[3] Jupiter's main auroral emission occurs over a narrow extent in latitude which maps to an equatorial distance of ~20–30 R_J [*Clarke et al.*, 2004]. At the atmosphere, *Gustin et al.* [2004] determined that the emission was excited by ~30–200 keV electrons from the ratio of emission at two UV wavelengths and a model of the atmosphere. This implies field-aligned potentials of a similar voltage, i.e., 30–200 kV. *Nichols and Cowley* [2004] explains these characteristics by including a Σ_P that is modified by the energy flux of the precipitating electrons. They determine the energy flux of the precipitating electrons by using the linear approximation of the *Knight* [1973] current-voltage relation as derived by *Lyons* [1980], which relates current density to the strength of the field-aligned potentials ($\Phi_{\parallel}$) based on the electron density and temperature of the equatorial population. However, *Nichols and Cowley* [2004] does not include the effects of field-aligned potentials when mapping the electric fields between the ionosphere and magnetosphere. The results of their model are in good agreement with many of the observed constraints, but the model requires radial mass transport rates ($\dot{M}$) of ~3000 kg/s to explain the observed radial currents of ~90 MA [*Khurana and Kivelson*, 1993; *Khurana*, 2001] and an equatorial mapping location for the main auroral oval of ~25 R_J.

[4] The presence of field-aligned potentials allows for differential rotation between the magnetosphere and ionosphere. One effect of the field-aligned potentials is to alter the electric field mapping between the ionosphere and magnetosphere. The field-aligned potentials can significantly affect angular momentum transport if the potential drops are comparable to the rotational potential [*Mauk et al.*, 2002]. Hubble observations of Jupiter's main auroral oval indicate an auroral

[1]Laboratory for Atmospheric and Space Physics, University of Colorado at Boulder, Boulder, Colorado, USA.

0148-0227/10/2010JA015423

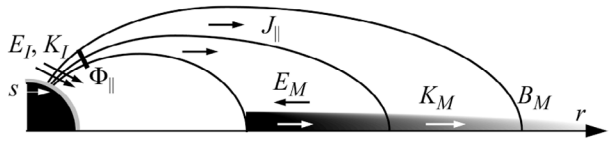

Figure 1. Diagram of coordinates and variables used in the model in the corotating frame. The model is 1-D, and all variables are a function of the radial position from the spin axis in the magnetosphere (r). The corresponding distance from the spin axis in the ionosphere is s. The magnetic field model is assumed to be aligned with the spin axis. The field-aligned potential, marked by the bar, is expected to develop close to Jupiter.

width on order 1000 km (Clarke, private communication, 2007) which maps to a magnetospheric width of ~15 R_J centered at a radial distance of ~25 R_J. The rotational potential in the reference frame of corotation derived from the integration of the magnetospheric electric field from our solution with a radial mass transport rate of 1000 kg/s (Figure 4) is ~212 kV across 15 R_J (from 20 R_J to 35 R_J) comparable to the field-aligned potentials indicated by precipitating auroral electrons [*Gustin et al.*, 2004].

[5] *Nichols and Cowley* [2005] examines the effects of field-aligned potentials on the transfer of angular momentum between Jupiter and the magnetosphere. Their analysis uses the linear approximation to the *Knight* [1973] relation developed by *Lyons* [1980] to determine $\Phi_\parallel$ and holds the Pedersen conductivity constant. They find that the impact of field-aligned potentials on the transport of angular momentum from the ionosphere to the magnetosphere is negligible to third order, justifying their omission of field-aligned potentials in the electric field mapping for the *Nichols and Cowley* [2004] analysis.

[6] This result, however, depends on the current-voltage relation. The *Knight* [1973] current-voltage relation assumes a constant electric field, and hence monotonic potential structure, between the plasma sheet and ionosphere. The electron temperature and density are fixed to values in the plasma sheet and the motion of the electrons along the flux tube is dictated by mirror forces. *Lyons* [1980] finds that the *Knight* [1973] current-voltage relation could be approximated linearly in the regime where $1 \ll e\Phi_\parallel/kT_e \ll R_x(R_x(r)$ is the mirror ratio at the top of the acceleration region). That is, the electron potential energy is greater than the electron thermal energy, but not to the extent that the electron distribution function is appreciably depleted.

[7] *Ray et al.* [2009] shows that the current-voltage relation for a centrifugally confined plasma must take into account the location of the acceleration region and the properties of the plasma at high latitudes. Jupiter's rapid rotation rate (period ~9.8 h) results in the centrifugal confinement of ions to the equatorial plane. The electrons are then confined by an ambipolar electric field which maintains quasi-neutrality [*Melrose*, 1967; *Hill et al.*, 1974]. The confinement of magnetospheric plasma results in a low-density plasma at high latitudes, the location of which coincides with the minimum in the sum of gravitational and centrifugal potentials. *Ray et al.* [2009] uses a 1-D spatial, 2-D velocity space Vlasov code developed by *Ergun et al.* [2000] and *Su et al.* [2003] to determine the current-voltage relationship that develops due to the equatorial confinement of plasma and subsequent lack of current carriers at high latitudes. The analysis looks at the flux tube downstream from Io which intersects the equatorial plane at a radial distance of ~5.9 R_J. The resulting current-voltage relation has an analytic expression similar to that derived by *Knight* [1973], but takes into account the high-latitude plasma properties and location of the acceleration region. The *Knight* [1973] relation overestimates the saturated current densities derived by the *Ray et al.* [2009] model by 2 orders of magnitude for identical values of field-aligned potential.

[8] *Ergun et al.* [2009] investigates the current system which develops in the wake region downstream of Io, accelerating the newly picked-up plasma up to corotation. Their analysis includes the full current circuit, i.e., the upward and downward current regions. Field-aligned potentials are self-consistently included in the electric field mapping, along with the modification of the Pedersen conductivity by precipitating electrons. The current density is related to the field-aligned potentials using the "high-latitude current choke" current-voltage relation described by *Ray et al.* [2009]. *Ergun et al.* [2009] finds that including field-aligned potentials in the circuit does not appreciably change the net transfer of angular momentum, however it spreads the transfer out over a broader radial range than previous solutions. The time scale for the acceleration of the wake plasma to corotation is consistent with solutions that do not include field-aligned potentials [*Hill and Vasyliūnas*, 2002]. However, the field-aligned potentials which develop in the middle magnetosphere (30–200 kV) are much larger than those in the Io wake region (100s V to 1 kV as inferred from *Bonfond et al.* [2009]) and hence *Ergun et al.* [2009] postulates that field-aligned potentials will have a more significant effect in the middle magnetosphere.

[9] Our model investigates the upward current system that is set up by the radial plasma transport. The location of the downward current region is unclear. *Cowley and Bunce* [2001] states that the downward current region is at the magnetopause which they placed at 100 R_J. However, data and observations suggest that the downward current region exists inside the magnetopause boundary [*Khurana*, 2001; *Kivelson et al.*, 2002]. *Khurana* [2001] uses Galileo data to map the divergence of the height-integrated perpendicular currents throughout Jupiter's magnetosphere. His analysis finds a downward current region between 08:00 and 13:00 LT over radial distances of ~25 to 50 R_J. *Kivelson et al.* [2002] finds evidence of return current flow at the magnetopause in Galileo observations. *Radioti et al.* [2008] suggests that this region of return current corresponds to the discontinuity in Jupiter's main auroral emission which is fixed in local time and observed in the prenoon and early noon sectors. *Mauk and Saur* [2007] measure spatial and temporal structure in the Galileo EPD data which suggests that there are downward current regions adjacent to upward current regions in Jupiter's middle magnetosphere. These downward current regions map to auroral regions at Jupiter. For simplicity, we model the magnetosphere out to 100 R_J, but do not include the downward current region. As we do not include the entire circuit, we cannot fully balance sources and sinks of energy. Therefore we do not have a global energy equation for the system and, because of this, our model is underconstrained, resulting in a set of solutions.

Table 1. Symbols and Parameters Used in the Model

Symbol	Description	Type	Units
$\alpha(r)$	Magnetosphere-ionosphere radial field mapping	Prescribed	–
$B_M(r)$	Magnetic field in magnetosphere	Prescribed	T
$E_I(r)$	Ionospheric electric field (north) in corotating frame	Variable	V m^{-1}
$E_M(r)$	Magnetospheric electric field (radial) in corotating frame	Variable	V m^{-1}
$E_I^*(r)$	Ionospheric electric field (north) mapped to the magnetosphere	Variable	V m^{-1}
$\Phi_\parallel(r)$	Field-aligned potential between ionosphere and magnetosphere	Variable	V
$J_\parallel^M(r)$	Field-aligned current density at the magnetosphere	Variable	A m^{-2}
$J_\parallel^I(r)$	Field-aligned current density at the ionosphere	Variable	A m^{-2}
$K_I(s)$	Height-integrated current (ionosphere)	Variable	A m^{-1}
$K_M(r)$	Height-integrated current (magnetosphere)	Variable	A m^{-1}
$\dot{M}$	Radial transport rate of plasma mass from Io torus	Constant	kg s^{-1}
r	Equatorial radial position in magnetosphere	Ordinant	m
$R_M(r)$	Magnetic mirror ratio	Prescribed	–
$s(r)$	Radial distance from spin axis at the ionosphere	Variable	m
Σ_P	Height-integrated Pedersen conductivity	Variable	Ω^{-1}
$\Omega(r)$	Local rotation rate	Variable	s^{-1}
Ω_J	Jupiter's ionospheric rotation rate	Constant	s^{-1}
$\omega(r)$	Deviation from corotation: $\Omega(r) - \Omega_J$	Variable	s^{-1}

[10] There are two significant differences between our model and that of *Nichols and Cowley* [2005]. Our model uses the "high-latitude current choke" current-voltage relation described by *Ray et al.* [2009] instead of a linear approximation to the Knight relation. Another difference is that *Nichols and Cowley* [2005] find a "relaxed" solution which determines the Hill solution for the magnetosphere and then accounts for the effects of the field-aligned potential. Our model merges the physics described in the work of *Nichols and Cowley* [2004, 2005] by both self-consistently including field-aligned potentials in the electric field mapping and varying the Pedersen conductivity with electron precipitation.

[11] The large $\dot{M}$ of 3000 kg/s that *Nichols and Cowley* [2004] need to match observational constraints is nearly an order of magnitude larger than the ~500 kg/s determined by chemistry based models constrained by spacecraft observations [*Delamere et al.*, 2005]. *Delamere et al.* [2005] shows that a neutral source rate of ~700–1200 kg/s from Io, which is then ionized, matches the Cassini UVIS data for the Io plasma torus. However, roughly half of this is removed from the system through charge exchange and fast neutral escape leaving ~350–600 kg/s of plasma that is then transported radially outward. For this analysis we pick 1000 kg/s as the typical value for the radial outflow from the torus in order to compare our model with previous analyses. We also investigate the transfer of angular momentum for $\dot{M}$ = 500 kg/s, which is more consistent with observations.

[12] Motivated to explain the narrow auroral width, corotation breakdown at ~20 R_J, auroral equatorial mapping distance of ~20–30 R_J, and large radial currents with a smaller $\dot{M}$, we investigate the impact of including field-aligned potentials ($\Phi_\parallel$) in the magnetosphere-ionosphere coupling system that results from radial outflow in Jupiter's magnetosphere.

2. System of Equations

[13] We start with the same set of equations used in previous models [*Pontius and Hill*, 1982; *Nichols and Cowley*, 2004]. All symbols are described in Table 1, and Figure 1 shows the geometry. All variables are a function of radial distance in the equatorial plane as our model is 1-D and assumes that the magnetic field is aligned with the spin axis. The model also assumes that Jupiter's ionosphere and plasma sheet are infinitely thin and cylindrically symmetric.

2.1. Magnetic Field Model and Mapping Function

[14] We incorporate the CAN-KK magnetic field model [*Cowley and Bunce*, 2001; *Nichols and Cowley*, 2004, 2005] which joins the *Connerney et al.* [1981] magnetic field model (CAN) and the *Khurana and Kivelson* [1993] magnetic field model (KK). The CAN model is derived from Voyager-1 and Pioneer-10 data and applied at distances close to Jupiter ($r <$ 21.78 R_J) while the KK model is determined using Voyager-1 data and applied at distances farther from Jupiter ($r >$ 21.78 R_J). The CAN-KK model assumes no tilt relative to the spin axis and has an equatorial plasma sheet. The north-south component of the equatorial field, B_M, is defined as follows [*Nichols and Cowley*, 2004, 2005]

$$B_M(r) = -\left\{ B_0 \left(\frac{R_J}{r}\right)^3 \exp\left[-\left(\frac{r}{r_0}\right)^{5/2}\right] + A\left(\frac{R_J}{r}\right)^m \right\} \quad (1)$$

where $B_0 = 3.335 \times 10^5$ nT, $r_0 = 14.501$ R_J, $A = 5.4 \times 10^4$ nT, and $m = 2.71$. The corresponding flux function in the equator is determined by integrating

$$B_M(r) = \frac{1}{r}\frac{dF_e(r)}{dr} \quad (2)$$

which yields [*Nichols and Cowley*, 2004, 2005]

$$F_e(r) = F_\infty + \frac{B_0 R_J^3}{2.5 r_0}\Gamma\left[-\frac{2}{5}, \left(\frac{r}{r_0}\right)^{5/2}\right] + \frac{A R_J^2}{(m-2)}\left(\frac{R_J}{r}\right)^{m-2} \quad (3)$$

where $F_\infty \approx 2.841 \times 10^4$ nT R_J^2 is the value of the flux function at infinity and $\Gamma(a, z)$ is the incomplete gamma function. The flux function at the ionosphere is

$$F_i = B_J s^2 = B_J R_J^2 \sin^2\theta \quad (4)$$

where s is the distance from the spin axis to the edge of the planet. The magnetic flux is constant along a given flux shell and therefore the magnetic mapping between the ionosphere and magnetosphere is defined as $F_i = F_e$. The ionospheric colatitude is then defined as

$$\sin\theta_i = \sqrt{\frac{F_e(r)}{B_J R_J^2}} \quad (5)$$

where $B_J = 4.25 \times 10^5$ nT is the equatorial magnetic field strength at Jupiter (Figure 2). Combining equations (4) and

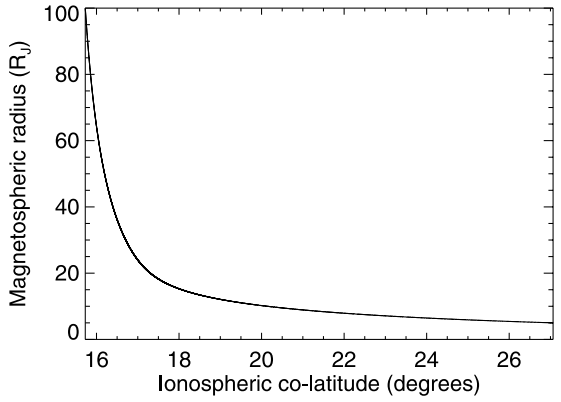

Figure 2. Mapping relationship between ionospheric colatitude and magnetospheric radius.

(5) the distance, $s(r)$, in meters, from the spin axis to the edge of the planet at the ionosphere can be rewritten as

$$s(r) = R_J\sqrt{\frac{F_e(r)}{B_J}} \tag{6}$$

The dimensionless mapping function, $\alpha(r)$, is then defined by conservation of magnetic flux as

$$\alpha(r) = \frac{B_I(r)s(r)}{B_M(r)r} \tag{7}$$

where B_I is the magnetic field strength at the ionosphere which we approximate to be that given by a dipole field:

$$B_I(r) = B_J\left(1 + 3\cos^2\theta_i\right)^{1/2} \tag{8}$$

2.2. Currents, Electric Fields, and Angular Velocity

[15] All calculations are made in Jupiter's corotating reference frame where the electric field represents deviation from corotation. In the frame of corotation, the magnetosphere is the magnetohydrodynamic (MHD) generator and the source of Poynting flux ($\mathbf{E}\cdot\mathbf{J} < 0$). Following the analyses of *Hill* [1979], *Pontius* [1997], and *Nichols and Cowley* [2004, 2005] we begin with torque balance in the equatorial plane between the outward moving plasma and the $\mathbf{J}\times\mathbf{B}$ force from the subsequent currents:

$$\dot{M}\frac{d}{dr}\left(r^2\Omega(r)\right) = 2\pi r^2 K_M(r)B_M(r) \tag{9}$$

The radial mass transport rate, $\dot{M}$, is assumed to be constant through the system as charge exchange is localized near Io's orbit. $K_M(r)$ represents the magnetospheric height-integrated current density (A/m) and

$$\Omega(r) = \Omega_J + \omega(r) \tag{10}$$

where $\omega(r)$ is the deviation in the angular velocity from corotation, Ω_J is the angular velocity of Jupiter, and $\Omega(r)$ is the total angular velocity of the magnetospheric plasma. Any deviation in the angular velocity from corotation results in an electric field in the magnetosphere. The magnetospheric electric field is calculated in the corotating frame by

$$E_M(r) = \omega(r)rB_M(r) \tag{11}$$

As the magnetic field lines are initially assumed to be equipotentials, the magnetospheric electric field (E_M) maps directly to the ionospheric electric field (E_I) in steady state ($\vec{\nabla}\times\vec{E} = 0$) using

$$E_I(r) = \alpha(r)E_M(r) \tag{12}$$

The mapping function, $\alpha(r)$, for the CAN-KK magnetic field model ranges from ~20 at 5 R_J to ~11000 at 100 R_J. The height integrated ionospheric current density, K_I, is determined using Ohm's law for a given height-integrated Pedersen conductivity, Σ_P, yielding

$$K_I(r) = \Sigma_P E_I(r) \tag{13}$$

We then map the height-integrated ionospheric current density out to the equatorial plane to determine the height-integrated magnetospheric current density, K_M, by

$$K_M(r) = -2K_I(r)\frac{s(r)}{r} \tag{14}$$

We assume that both hemispheres respond identically accounting for the factor of two.

[16] The field-aligned current density at the magnetosphere, $J_\parallel^M(r)$, is determined through current continuity

$$J_\parallel^M(r) = \frac{1}{r}\frac{d}{dr}\left(\frac{rK_M(r)}{2}\right) \tag{15}$$

with the ionospheric field-aligned current density then defined as

$$J_\parallel^I(r) = R_M(r)J_\parallel^M(r) \tag{16}$$

which is the field-aligned current density at the magnetosphere, $J_\parallel^M(r)$, times the mirror ratio between the ionosphere and magnetosphere, $R_M(r)$.

[17] Equations (9)–(14) form the basis of the conductance-dominated solutions which ignore $\Phi_\parallel$, hold Σ_P constant (equation (13)) and were initially solved by *Hill* [1979] using a dipole magnetic field and modified by *Pontius* [1997] to include a stretched magnetic field configuration. Later, *Nichols and Cowley* [2004] solved the same set of equations with a variable conductance and a stretched magnetic field. The Pedersen conductivity was based on the *Millward et al.* [2002] model which *Nichols and Cowley* [2004] modified to account for varying electron precipitation energy. The Pedersen conductivity was then expressed as a function of $J_\parallel^I$ through use of the linear approximation to the *Knight* [1973] relation. However, the effects of $\Phi_\parallel$ were not considered in the electric field mapping between the ionosphere and the magnetosphere. Following *Nichols and Cowley* [2005], we modify the mapping of the ionospheric and magnetospheric electric fields to self-consistently include a field-aligned potential. Equation (12) ($\vec{\nabla}\times\vec{E} = 0$) is modified as

$$E_I(r) = \alpha(r)\left(E_M(r) - \frac{d\Phi_\parallel(r)}{dr}\right) \tag{17}$$

for a steady state, upward current system. The term $d\Phi_{\parallel}/dr$ represents the radial derivative of the field-aligned potential between the ionosphere and magnetosphere (i.e., the perpendicular derivative of the parallel potential). The derivative is evaluated in the equatorial plane. We also define a new variable

$$E_I^*(r) = E_I(r)/\alpha(r) \tag{18}$$

to represent the ionospheric electric field mapped to the magnetosphere. This mapped ionospheric electric field is important for direct comparisons between the magnetosphere and ionosphere, especially when the magnetic field lines are not equipotentials.

[18] A current-voltage relation is required to include self-consistently the effects of $\Phi_{\parallel}$ on the field-aligned current density. As the field-aligned potential grows, the electron distribution moves into the loss cone, increasing the number of current carriers that can reach the ionosphere and hence increasing the field-aligned current density. Once the electron distribution is completely in the loss cone the field-aligned current density is saturated and can no longer grow with increases in the field-aligned potential. Following *Ray et al.* [2009] we use the "high-latitude current choke" current voltage relation

$$J_{\parallel}^I(r) = j_x + j_x(R_x - 1)\left(1 - e^{-\left(\frac{e\Phi_{\parallel}(r)}{T_x(R_x-1)}\right)}\right) \tag{19}$$

where $J_{\parallel}^I$ is the field-aligned current density at the ionosphere, $j_x = en_x\sqrt{T_x/(2\pi m_e)}$ is the electron thermal current density, R_x is the magnetic mirror ratio at the top of the acceleration region (located 2–3 R_J jovicentric), T_x is the electron temperature (expressed in units of energy), n_x is the electron density, m_e is the electron mass, and e is the fundamental charge. The subscript $(_x)$ indicates that the quantities are evaluated at the top of the acceleration region, which is located where the sum of the gravitational and centrifugal potentials along the flux tube is a minimum [*Ray et al.*, 2009]. The value of j_x at this location is hereafter referred to as the critical current density, J_{crit}. Equation (19) is valid only for $J_{\parallel}^I \geq J_{crit}$, otherwise we set $\Phi_{\parallel} = 0$ and $J_{\parallel}^I$ is calculated through equation (16).

[19] In addition to self-consistently including $\Phi_{\parallel}$ in the electric field mapping, once $J_{\parallel}^I \geq J_{crit}$ we also modify the Pedersen conductivity to vary with incident energy flux (EF) and precipitating electron energy at Jupiter's ionosphere such that equation (13) becomes

$$K_I(r) = \Sigma_P(\Phi_{\parallel}, EF)E_I(r) \tag{20}$$

We use a model based on that presented in the work of *Millward et al.* [2002], but modified so that Σ_P varies with both the incident electron flux and the precipitating energy of the electrons

$$\Sigma_P(\Phi, EF) = \Sigma_{P_0} + \epsilon\frac{\Sigma_{P_{\Phi_{\parallel}}}(\Phi_{\parallel})\Sigma_{P_{EF}}(EF)}{\Sigma_{P_{EF}}(10mW/m^2)} \tag{21}$$

where Σ_{P_0} is the height-integrated Pedersen conductivity in nonauroral regions, $EF = J_{\parallel}\Phi_{\parallel}$ is the incident energy flux at the auroral region, $\Phi_{\parallel}$ is the field-aligned potential, and ε is the efficiency of the Pedersen conductivity enhancement. $\Sigma_{P_{\Phi_{\parallel}}}(\Phi_{\parallel})$ and $\Sigma_{P_{EF}}(EF)$ are functions for the Pedersen conductivity with precipitating electron energy and incident energy flux derived from those in the work of *Millward et al.* [2002], respectively. The full details of the above Pedersen conductivity formulation are given in Appendix A. As in previous analyses [*Hill*, 1979], we set $\Sigma_{P_0} = 0.1$ mho and $\varepsilon = 1$ unless otherwise stated.

[20] Equations (9)–(11) and (13)–(19) represent a closed set that includes field-aligned potentials generated by field-aligned currents. These equations can be rewritten as two coupled differential equations, one which is second order in $\Phi_{\parallel}$ and first order in ω and one which is first order in $\Phi_{\parallel}$ and ω. This coupled set of equations can be numerically solved by setting three boundary conditions: (1) the initial deviation from corotation, ω_0; (2) the initial field-aligned potential, $\Phi_{\parallel 0}$; and (3) the initial radial gradient of the field-aligned potential, $\left(\frac{d\Phi_{\parallel}}{dr}\right)_0$.

3. Auroral Parameters

[21] The goal of our modeling is to explain the following observed properties of Jupiter's main auroral emission: the limited latitudinal extent of the aurora on order ~1000 km (Clarke, private communication, 2007) corresponding to ~1° at the atmosphere; a mean energy of precipitating electrons between ~30 and ~200 keV; and a mean energy flux from ~2 to ~30 mW/m^2 derived from ultraviolet images of Jupiter's main auroral oval [*Gustin et al.*, 2004]. The main auroral oval maps to equatorial distances between ~20 and 30 R_J as determined by the existence of near-corotational features [*Clarke et al.*, 2004]. In addition, Voyager data from a pass through the prenoon, dayside magnetosphere suggest a deviation from corotation at distances greater than 10 R_J [*McNutt et al.*, 1979], however the angular velocity profile does not decrease as quickly as that predicted by the *Hill* [1979] profile [*Belcher*, 1983, Figure 3.23].

[22] *Khurana* [2001] derives the height-integrated radial current as a function of local time between 15 and 75 R_J using Galileo Magnetometer data. We find an asymptotic radial current of ~86 MA using Figure 12 from *Khurana* [2001] and averaging across all local times at a radial distance of 25 R_J. We calculate the total asymptotic radial current at 25 R_J because of local time variations at larger radial distances [*Khurana*, 2001, Figure 12].

[23] In our model there are several values that must be prescribed including the magnetic field ($B_M(r)$, $\alpha(r)$, $R_M(r)$), the location of the acceleration region and associated plasma parameters (j_x, T_x, R_x), and the Pedersen conductivity in the absence of modification by particle precipitation (Σ_{P_0}). To compare with previous work [*Nichols and Cowley*, 2004], we use a high-latitude electron density of 0.01 cm^{-3} and an electron temperature of ~2.5 keV which are the temperature and density of the hot electron population at 17 R_J as measured by Voyager 1 [*Scudder et al.*, 1981]. This density and temperature yield a critical current of $J_{crit} \sim 0.01$ μAm^{-2}. Following *Ray et al.* [2009] and *Su et al.* [2003], the auroral cavity forms at ~2.5 R_J from the center of Jupiter at which distance the magnetic mirror ratio is ~16. The incident energy flux on the ionosphere, maximum field-aligned potential ($\Phi_{\parallel \mathrm{Max}}$, and total radial current at 100 R_J (I_{100}) are dependent

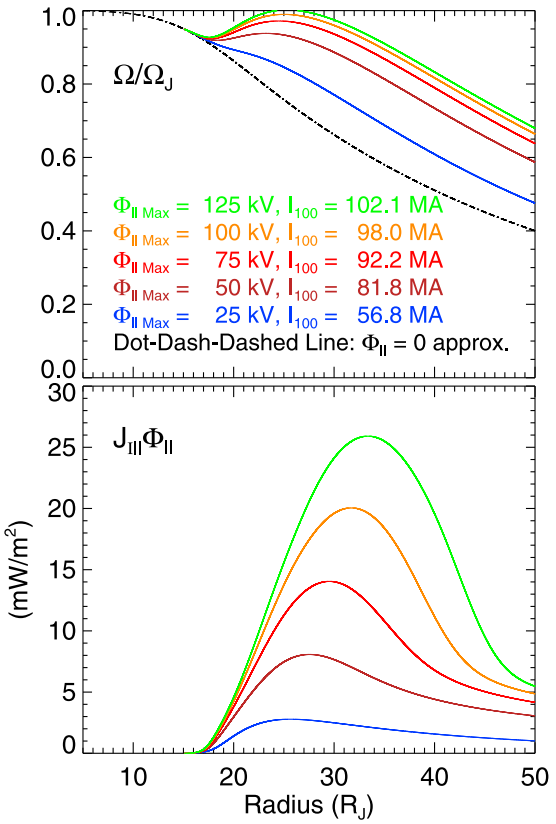

Figure 3. Sensitivity of the solutions to the chosen outer constraint. (top) The angular velocity of the magnetospheric plasma with the dot-dash-dashed lines displaying the $\Phi_{||} = 0$ approximation for comparison. (bottom) Incident energy flux on the atmosphere as a function of equatorial mapping location, corresponding to the brightness and width of the auroral emission.

properties dictated by the selection of independent parameters ($\dot{M}$, T_x, R_x, n_0, Σ_{P_0}) and boundary conditions (see section 4.1).

4. Numerical Solutions

[24] As described above, equations (9)–(11) and (13)–(19) present a set of coupled differential equations requiring three boundary conditions to solve (ω_0, $\Phi_{||0}$, and $\left(\frac{d\Phi_{||}}{dr}\right)_0$). We employ two numerical techniques, the "critical current technique," hereafter CCT, and the "constrained predictor-corrector," hereafter CPC, to determine the solutions to these equations.

[25] The CCT solves the $\Phi_{||} = 0$ approximation using equations (9)–(14). The solution to the $\Phi_{||} = 0$ approximation is generated by a modified Euler predictor-corrector scheme and starts with an initially corotating equatorial plasma ($\omega = 0$) at 5 R_J. Equation (9) is integrated to obtain ω, followed by the evaluation of equations (11)–(14). We determine $J_{||}^I$ via equation (16) but otherwise $J_{||}^I$ does not affect the calculations until the ionospheric current density is larger than the critical current density.

[26] At the location where the ionospheric current density first becomes larger than the critical current density, hereafter r_{crit}, we begin a solution which self-consistently includes the effects of the field-aligned potential in the electric field mapping and in variations of the Pedersen conductivity. The new solution is determined by equations (9)–(11) and (13)–(21) and we set our three boundary conditions, (ω_0, $\Phi_{||0}$, $\left(\frac{d\Phi_{||}}{dr}\right)_0$), at this location. The values of ω_0 and $\Phi_{||0}$ are determined by the solution to the $\Phi_{||} = 0$ approximation with $\Phi_{||0}$ calculated from $J_{||}^I$ using equation (19). The third boundary condition, $\left(\frac{d\Phi_{||}}{dr}\right)_0$, is selected by carrying out the $\Phi_{||} = 0$ approximation one step past r_{crit}, and calculating the resulting $\left(\frac{d\Phi_{||}}{dr}\right)_0$. The value of $\left(\frac{d\Phi_{||}}{dr}\right)_0$ predicted by the solution to the $\Phi_{||} = 0$ approximation is an initial guess as $\Phi_{||}$ is not yet self-consistently included in the physics of the calculation. After the initialization of the boundary conditions, the system is solved by alternating integration of equations (9) and (17).

[27] The inclusion of $\Phi_{||}$ results in a system of nonlinear equations which opens up the possibility of a set of solutions (Figure 3) subject to the selection of $\left(\frac{d\Phi_{||}}{dr}\right)_0$. The value of $\left(\frac{d\Phi_{||}}{dr}\right)_0$ must be further adjusted by setting an additional constraint such as I_{100}, $\Phi_{||Max}$, or the maximum energy flux incident on the ionosphere.

[28] As a consistency check, we calculate exact solutions using the CPC method described in Appendix B. This solution method integrates equations (9)–(11) and (13)–(19) radially outward from 5 R_J to 100 R_J using a continuous current-voltage relation which accounts for the downward field-aligned current due to outflowing ionospheric electrons in the absence of a field-aligned potential instead of equation (19). The alternative technique also requires that we select an outer constraint such as $\Phi_{||Max}$, I_{100}, or the maximum energy flux incident on the ionosphere as described above. The exact solutions found by this numerically intensive technique provide confidence in those found with the more approximate CCT.

[29] The following solutions are found using the CCT. All profiles are plotted as a function of radial distance in the equatorial plane including the profiles of ionospheric quantities (i.e., energy flux ($\Phi_{||}$ $J_{||}^I$), $J_{||}^I$, and $\Phi_{||}$). For the ionospheric quantities, the magnitudes plotted are those at the ionosphere, with the exception of E_I^* which by definition is a mapped quantity. We map ionospheric profiles to the equatorial plane for ease of comparison. We can then apply the mapping function, $\alpha(r)$, to determine the scale size of the profile variabilities at the ionosphere. A width of ~15 R_J in the equatorial plane centered at $r = 25$ R_J corresponds to an ionospheric width of 1000 km or ~1° (see Figure 2).

4.1. Boundary Condition Selection

[30] Figure 3 displays the solution dependence on the outer constraint for a range of $\Phi_{||Max}$. The angular velocity profile (top) and energy flux profile (bottom) are shown with the associated I_{100} for $\dot{M} = 1000$ kg/s, $\Sigma_{P_0} = 0.1$ mho, $T_x = 2.5$ keV, $n_0 = 0.01$ cm^{-3}, and $R_x = 16$. The maximum field-aligned potential and total radial current at 100 R_J are directly related and, as detailed above, dictate the value of $\left(\frac{d\Phi_{||}}{dr}\right)_0$. For the parameters given, $\left(\frac{d\Phi_{||}}{dr}\right)_0$ increases with the imposed $\Phi_{||Max}$. The relationship between $\Phi_{||}$, Σ_P, and $J_{||}^I$ is nonlinear,

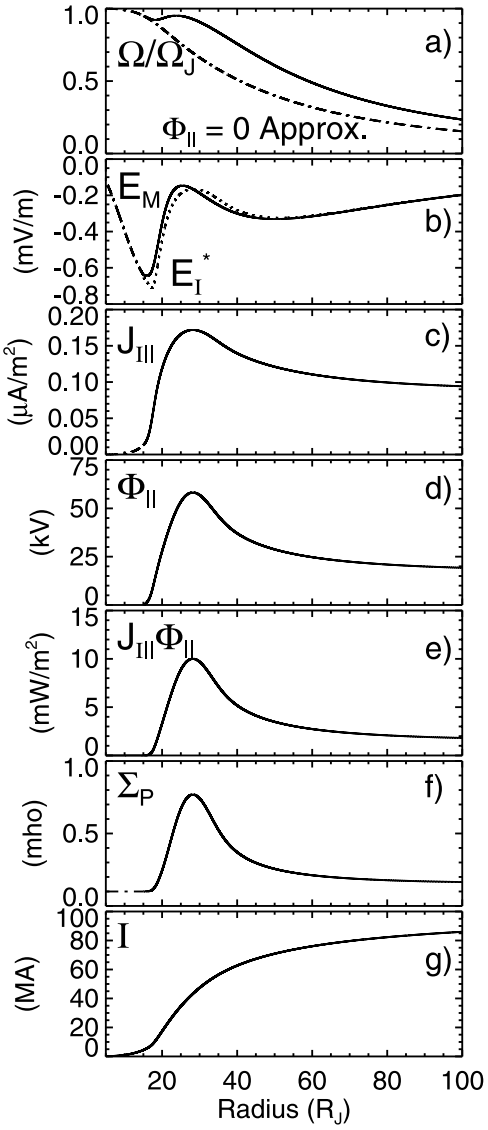

Figure 4. Model results for $\dot{M}$ = 1000 kg/s and Σ_{P_0} = 0.1 mho. (a) Rotation profile of plasma in the magnetosphere. The solution for the $\Phi_{||} = 0$ approximation profile is shown for reference (dashed-dotted line). (b–g) The magnetospheric (dashed line) and mapped ionospheric (solid line) electric fields, the current density in the ionosphere, the field-aligned potential, the incident energy flux at the ionosphere, the height-integrated Pedersen conductivity, and the total radial current.

therefore small differences in $\left(\frac{d\Phi_{||}}{dr}\right)_0$ result in large variations in the system behavior.

[31] The energy flux profile, which indicates the brightness and latitudinal extent of the auroral emission, is also directly related to $\Phi_{||Max}$, and hence I_{100}. Solutions with larger $\Phi_{||Max}$ have a brighter, wider auroral emission (bottom) with associated angular velocities that remain near corotation out to large radial distance. For this study, we choose I_{100} = 86 MA as determined from [*Khurana*, 2001] and discussed above.

4.2. Solution With $\dot{M}$ = 1000 kg/s, I_{100} = 86 MA

[32] Figure 4 presents the solutions for the case where $\dot{M}$ = 1000 kg/s, Σ_{P_0} = 0.1 mho, T_x = 2.5 keV, n_0 = 0.01 cm^{-3}, and R_x = 16. For this case we set I_{100} = 86 MA as our outer constraint and determine $\left(\frac{d\Phi_{||}}{dr}\right)_0$. Figure 4a displays the angular velocity of the magnetospheric plasma normalized to corotation. The dot-dash-dashed line displays the solution for the $\Phi_{||} = 0$ approximation for comparison. Figure 4b displays the magnetospheric and ionospheric electric fields (solid and dotted lines, respectively). Figures 4c–4g display the ionospheric current density, field-aligned potential, energy flux incident on the ionosphere, height-integrated Pedersen conductivity, and radial current, respectively.

[33] The critical radius for the parameters above is r_{crit} = 15.1 R_J. From this location outward, field-aligned potentials are self-consistently included. The field-aligned potential peaks at ~28 R_J. The magnitude of the mapped ionospheric electric field ($|E_I^*|$) is larger than that of the magnetospheric electric field where $d\Phi_{||}/dr$ is positive, and smaller than that of the magnetospheric electric field ($|E_M|$) where $d\Phi_{||}/dr$ is negative. Initially, $|E_I^*|$ grows when field-aligned potentials are included in the system.

[34] The field-aligned potentials boost the electron distribution into the loss cone increasing the field-aligned current density and accelerating electrons into the ionosphere; both effects of which enhance the ionospheric height-integrated Pedersen conductivity. As per Ohm's law (equation (20)) one of the following must occur if there is a sharp increase in Σ_P: the magnitude of the ionospheric electric field must decrease, the magnitude of the ionospheric height-integrated current density must grow, or both $|E_I^*|$ and K_I must vary. As both the ionospheric electric field and Pedersen conductivity vary with $\Phi_{||}$, both the magnitude of the ionospheric electric field decreases as Σ_P increases and the magnitude of K_I grows. It is important to note that enhancements in the Pedersen conductivity do not increase the field-aligned current density to the same degree as in previous models [e.g., *Nichols and Cowley*, 2004] because the magnitude of the ionospheric electric field can shift relative to that of the magnetospheric electric field when $\Phi_{||}$ is self-consistently included. The field-aligned potential, electron energy flux, and Pedersen conductivity all turn over at ~28 R_J.

[35] The $\mathbf{I} \times \mathbf{B}$ force in the equatorial plane increases with the field-aligned current density. The angular velocity of the plasma stays near corotation until ~30 R_J. Past ~30 R_J the $\mathbf{I} \times \mathbf{B}$ force is too weak to keep the plasma near corotation as the north-south component of the equatorial magnetic field decreases with radial distance, and the plasma angular velocity declines following a profile similar to that of the $\Phi_{||} = 0$ approximation.

[36] The above parameters result in a main auroral emission that maps to 28 R_J with a half-width of ~10 R_J. The maximum energy flux and electron precipitation energy are ~10 mW/m^2 and ~60 keV, respectively, and are consistent with the energy fluxes and electron precipitation energies derived from HST observations.

4.3. Solution with $\dot{M}$ = 500 kg/s, I_{100} = 86 MA

[37] Figure 5 presents the solutions for the case where $\dot{M}$ = 500 kg/s, Σ_{P0} = 0.05 mho, T_x = 2.5 keV, n_0 = 0.01 cm^{-3}, and

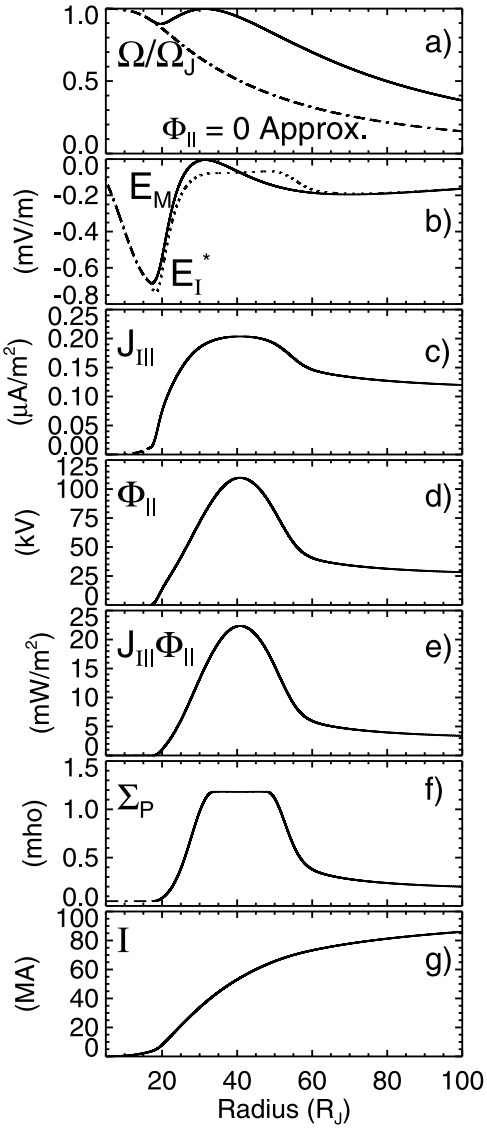

Figure 5. Model solutions for $\dot{M}$ = 500 kg/s and Σ_{P_0} = 0.05 mho. (a) Rotation profile of plasma in the magnetosphere. The solution for the $\Phi_{||}$ = 0 approximation profile is shown for reference (dashed-dotted line). (b–g) The magnetospheric (dashed line) and mapped ionospheric (solid line) electric fields, the current density in the ionosphere, the field-aligned potential, the incident energy flux at the ionosphere, the height-integrated Pedersen conductivity, and the total radial current.

R_x = 16. As in the $\dot{M}$ = 1000 kg/s case, I_{100} = 86 MA. Figure 5a displays the angular velocity of the magnetospheric plasma normalized to corotation. The dot-dash-dashed line displays the solution for the $\Phi_{||}$ = 0 approximation for comparison. Figure 5b displays the magnetospheric and ionospheric electric fields (solid and dotted lines, respectively). Figures 5c–5g display the ionospheric current density, field-aligned potential, energy flux incident on the ionosphere, height-integrated Pedersen conductivity, and radial current, respectively.

[38] The critical radius for the above parameters is r_{crit} = 17.3 R_J. From this location outward, field-aligned potentials are self-consistently included in the calculation. The general profile behavior of the displayed parameters are similar to those for the $\dot{M}$ = 1000 kg/s case.

[39] The peak field-aligned potential is ~115 kV at ~40 R_J. The field-aligned current density grows with $\Phi_{||}$, increasing the upward currents and hence the **I** × **B** force in the magnetosphere. The magnetospheric plasma remains near corotation until ~35 R_J where the angular velocity begins to decrease, following a profile similar to that of the $\Phi_{||}$ = 0 approximation.

[40] When field-aligned potentials are self-consistently included, E_M and E_I no longer map directly. The magnitude of the magnetospheric electric field decreases, nearing zero as the plasma is accelerated toward corotation due to the increased **I** × **B** force. While $|E_M|$ decreases, $|E_I^*|$ grows until ~20 R_J where the magnitude of the ionospheric field begins to decrease due the enhancement in Σ_P. The ionospheric height-integrated current density increases as the growth of the Pedersen conductivity is stronger than the decline of $|E_I^*|$. The flattening of the $|E_I^*|$ and Σ_P profiles occurs when the field-aligned potential is greater than ~80 kV as the precipitating electrons have sufficient energy to penetrate through the peak Pedersen conducting layer, no longer enhancing the Pedersen conductance.

[41] The main auroral emission maps to an equatorial radius of ~40 R_J for an $\dot{M}$ of 500 kg/s. This peak is farther from Jupiter than predicted by HST observations. The peak energy flux is ~23 mW/m^2, consistent with auroral parameters derived from HST observations.

4.4. Effect of the Pedersen Conductivity Feedback

[42] As described in Appendix A and detailed in equation (21), the Pedersen conductivity function includes a factor, ε, which controls the efficiency of the enhancement of Σ_P with electron precipitation energy and incident energy flux. Figure 6 displays solutions with $\dot{M}$ = 1000 kg/s, R_x = 16, Σ_{P_0} = 0.1 mho, n_0 = 0.01 cm^{-3}, T_x = 2.5 keV, and $\Phi_{||\mathrm{Max}}$ = 75 kV, for efficiencies of 0.0, 0.1, 0.2, 0.5, 1.0, and 2.0. Figures 6a–6e show the normalized **I** × **B** force, field-aligned current density, angular velocity of the magnetospheric plasma, energy flux incident on the ionosphere, and radial current. The dot-dash-dashed lines displays the solution to the $\Phi_{||}$ = 0 approximation for comparison. Table 3 summarizes the key auroral parameters.

[43] The most prominent feature is that the **I** × **B** force in the equatorial plane increases and peaks nearer to Jupiter with increased efficiency of the Pedersen conductivity enhancement. The field-aligned current density (Figure 6b) at the ionosphere peaks at the same value for all solutions with nonzero ε, as $\Phi_{||\mathrm{Max}}$ is held fixed. However, the growth of $J_{||}^I$ occurs over a narrower radial range for larger ε. Therefore, for a given equatorial field strength, $J_{||}^I$ is larger for greater ε, resulting in a stronger **I** × **B** force. Subsequently, the magnetospheric plasma remains near corotation out to larger equatorial distances for stronger ε as seen in Figure 6c and Figure 7.

[44] Figure 8 shows the fractional percentage of the perpendicular gradient of the parallel potential to the corotational electric field $\frac{d\Phi_{||}/dr}{E_M}$ for ε = 0.0, 0.1, 0.2, 0.5, and 1.0. As the efficiency of the Pedersen conductivity feedback increases, and hence the **I** × **B** force on the magnetospheric plasma,

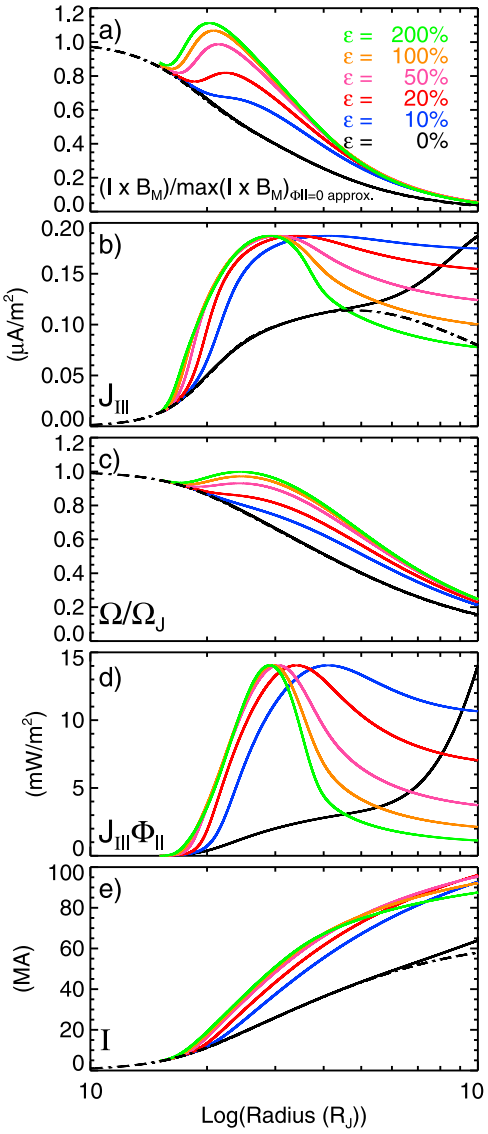

Figure 6. Effect of the Pedersen conductivity for $\Phi_{\|\mathrm{Max}}$ = 75 kV for feedback efficiencies of 0%, 10%, 20%, 50%, 100%, and 200%. (a–e) Normalized **I** × **B** force in the equatorial plane, the field-aligned current at the ionosphere, the angular velocity profile of the magnetospheric plasma, the energy flux incident on the ionosphere, and the radial current, respectively. The dashed-dotted line is the solution to the $\Phi_{\|}$ = 0 approximation for comparison.

$d\Phi_{\|}/dr$ becomes a larger, nonnegligible percentage of E_M. For a magnetospheric plasma accelerated back to perfect corotation, $\frac{d\Phi_{\|}/dr}{E_M}$ goes to negative infinity. For the nominal case of Σ_P feedback where $\varepsilon = 1$, $d\Phi_{\|}/dr$ is ~90% of E_M at its maximum, the location of which coincides with the location where the plasma angular velocity peaks as it is accelerated toward corotation. As the magnetic field strength, field-aligned current densities, and hence the **I** × **B** force decrease with equatorial radius, $|E_M|$ grows. The field-aligned potential profiles turns over, with $\frac{d\Phi_{\|}/dr}{E_M}$ going through zero and becoming positive as the field-aligned potentials decrease with radial distance. Inside ~30 R_J, $d\Phi_{\|}/dr$ is a small fraction of E_M for the $\varepsilon = 0$ case, therefore the field-aligned potentials do not significantly alter the electric field mapping and the angular velocity profile is similar to that of the $\Phi_{\|}$ = 0 approximation. In addition, the field-aligned current density for the $\varepsilon = 0$ case does not increase beyond that of the $\Phi_{\|} = 0$ approximation until the magnetic field strength is too weak to provide a significant **I** × **B** force. It is important to note that the $\Phi_{\|}$ = 0 approximation does not account for a lack of current carriers at high latitudes, and therefore draws similar field-aligned currents to the ε = 0 solution. A more representative solution would limit $J_{\|}^{I}$ at J_{crit} in the absence of

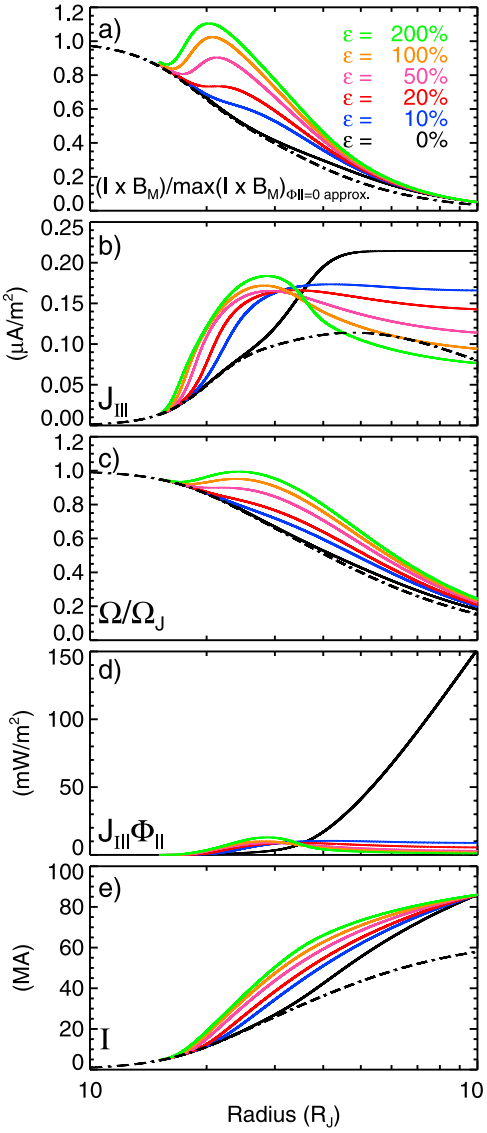

Figure 7. Effect of the Pedersen conductivity for I_{100} = 86 MA for feedback efficiencies of 0%, 10%, 20%, 50%, 100%, and 200%. (a–e) The normalized **I** × **B** force in the equatorial plane, the field-aligned current at the ionosphere, the angular velocity profile of the magnetospheric plasma, the energy flux incident on the ionosphere, and the radial current respectively. The dashed-dotted line is the solution to the $\Phi_{\|}$ = 0 approximation for comparison.

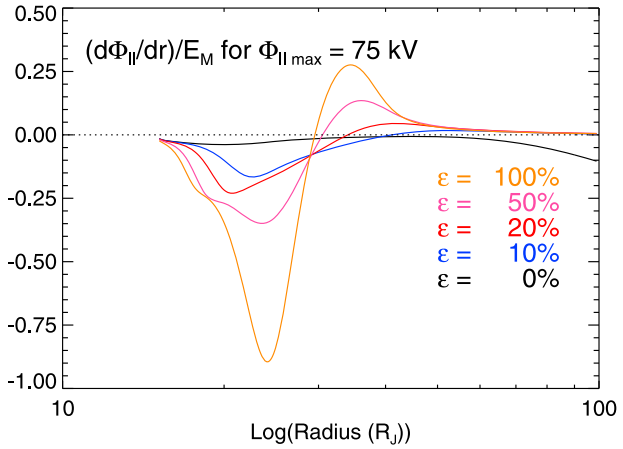

Figure 8. Fractional percentage of the perpendicular gradient of the parallel potential ($d\Phi_{\parallel}/dr$) to the corotational electric field (E_M) in the corotational frame. Profiles are shown for a $\Phi_{\parallel Max}$ of 75 kV and Pedersen conductivity feedback efficiencies of 0%, 10%, 20%, 50%, and 100%.

$\Phi_{\parallel}$, however this would not reproduce previous solutions [*Hill*, 1979; *Pontius*, 1997; *Nichols and Cowley*, 2004].

[45] The efficiency of the enhancement of Σ_P also alters the width and mapping location of the auroral emission. The auroral emission width is inversely related to ε with a stronger Σ_P enhancement leading to a narrower auroral oval. The equatorward edge of the emission remains roughly the same for $\varepsilon = 0.5$, 1.0, and 2.0, but the poleward boundary extends to higher latitudes. For ε = 0.1 and 0.2, the auroral emission extends to a width of ~2° latitude, reaching the outer boundary of our model.

[46] The incident electron energy flux at the atmosphere, and hence auroral brightness, does not change with ε in Figure 6 as the field-aligned current densities peak at the same value and we hold $\Phi_{\parallel Max}$ fixed at 75 kV. The field-aligned potentials and field-aligned current densities peak in the same region of the magnetosphere as shown in Figures 4 and 5, resulting in the same maximum electron energy flux for the efficiencies shown.

[47] Figure 7 displays the solutions for $\varepsilon = 0.0$, 0.1, 0.2, 0.5, 1.0, 2.0 with I_{100} = 86 MA. The key auroral parameters are summarized in Table 2. Unlike the case where the $\Phi_{\parallel Max}$ is held fixed, the peak incident electron energy flux varies with ε. The variation is nonlinear, with the minimum peak electron flux occurring for ε = 0.5. At low efficiencies (ε = 0.1, 0.2),

Table 2. Variation in Modeled Auroral Parameters With the Efficiency of the Pedersen Conductivity Enhancement (ε) for I = 86 MA, $\Sigma_{P_0} = 0.1$ mho, $R_x = 16$, $T_e = 2.5$ keV, $n_0 = 0.01$ cc^{-1}

ε	Max. EF (mW/m^2)	Max. $\Phi_{\parallel}$ (kV)	Equation Location (R_J)	Max. Ω/Ω_J (%)
0.0	151.6	706.7	–	–
0.1	10.3	59.6	41.9	94.9
0.2	8.9	53.5	33.8	94.9
0.5	8.7	52.8	29.1	94.9
1.0	10.0	58.2	28.2	95.1
2.0	12.9	70.3	28.7	99.4

Table 3. Variation in Modeled Auroral Parameters With the Efficiency of the Pedersen Conductivity Enhancement (ε) for $\Phi_{\parallel_{Max}} = 75$ kV, $\Sigma_{P_0} = 0.1$ mho, $R_x = 16$, $T_e = 2.5$ keV, $n_0 = 0.01$ cc^{-1}

ε	Max. EF (mW/m^2)	I_{100} (MA)	Equation Location (R_J)	Max. Ω/Ω_J (%)
0.0	14.0	63.9	–	–
0.1	14.0	92.7	41.1	94.9
0.2	14.0	96.0	34.0	94.9
0.5	14.0	95.5	30.5	94.9
1.0	14.0	92.2	29.5	97.2
2.0	14.0	87.5	29.0	99.8

the enhancement in the current density occurs over a broader radial range. The imposed outer constraint of I_{100} = 86 MA requires large field-aligned currents throughout the magnetosphere, resulting in a larger $\Phi_{\parallel Max}$ for low efficiencies. This interplay increases the peak electron energy flux incident on the atmosphere relative to the ε = 0.5 case, but moves the equatorial auroral oval mapping location out from Jupiter. For high efficiencies (ε = 1.0, 2.0) the enhancement in Σ_P increases the field-aligned current density over a narrower radial range. The magnitude of the ionospheric electric field grows relative to that of the magnetospheric electric field with the increase in Σ_P and K_I, which is reflected in the large $\Phi_{\parallel Max}$. The incident electron energy flux is larger than in the ε = 0.5 case and the equatorial mapping location of the main auroral oval moves in toward Jupiter. The auroral width follows the same trend as with the $\Phi_{\parallel Max}$ = 75 kV case, broadening with decreasing ε (Table 3).

4.5. Variations With Location of the Auroral Acceleration Region

[48] Figure 9 displays the variation in the solutions with $\dot{M}$ = 1000 kg/s, $\Sigma_{P_0} = 0.1$ mho, $n_0 = 0.01$ cm^{-3}, $T_x = 2.5$ keV, and an outer constraint of I_{100} = 86 MA for a variety of locations of the auroral acceleration region (R_x = 11, 16, 21, and 27 corresponding to distances along the flux tube of ~2.2, 2.5, 2.7, and 3 R_J jovicentric, respectively). Figures 9a–9e show the normalized **I** × **B** force, field-aligned current density, angular velocity of the magnetospheric plasma normalized to corotation, energy flux incident on the ionosphere, and height integrated Pedersen conductivity. The dot-dash-dashed lines display the solution to the $\Phi_{\parallel}$ = 0 approximation for comparison. The boundary condition $\left(\frac{d\Phi_{\parallel}}{dr}\right)_0$ is inversely related to R_x, with the largest $\left(\frac{d\Phi_{\parallel}}{dr}\right)_0$ for the case where R_x = 11 and the smallest for R_x = 27. The solutions for R_x = 16, 21, and 27 follow the result presented in section 4.2, while the solution for R_x = 11 is significantly different from that previously presented. The key auroral parameters are summarized in Table 4 for each case.

[49] For R_x = 11, $J_{\parallel}^I$ grows steeply over a narrow radial range and then plateaus at ~21 R_J, finally declining again ~50 R_J. The steep initial growth of $J_{\parallel}^I$ with radial distance occurs closer to Jupiter than in the other cases, where the equatorial magnetic field is stronger. Therefore the corresponding **I** × **B** force is larger than in the other cases as seen in Figure 9a. In the region from ~21–50 R_J, the field-aligned current density is saturated as the entire electron distribution has been moved into the loss cone. The field-aligned potential continues to increase, modifying the Pedersen conductance.

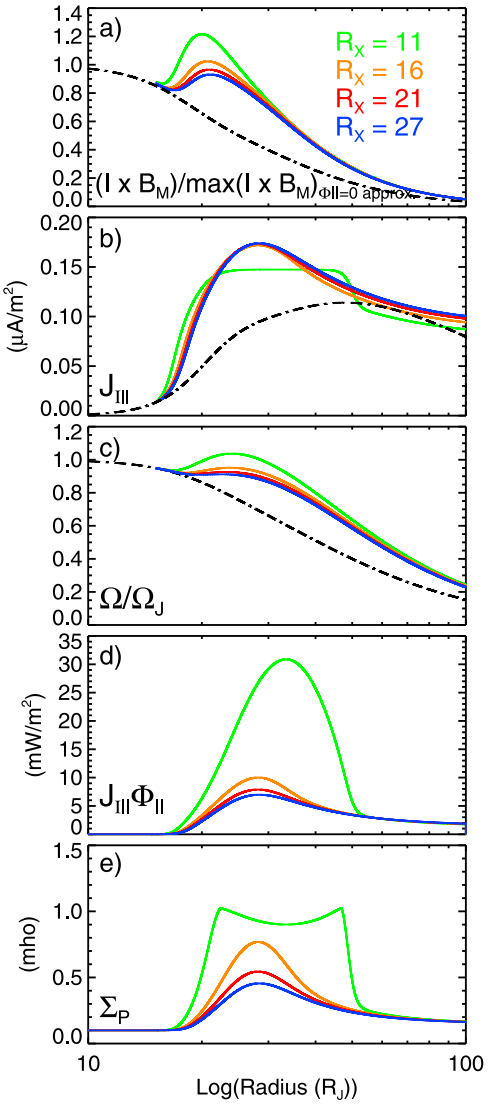

Figure 9. Solutions for varying acceleration region locations with magnetic mirror ratios of R_x = 11, 16, 21, and 27. (a–e) The normalized **I** × **B** force in the equatorial plane, the field-aligned current at the ionosphere, the angular velocity profile of the magnetospheric plasma, the energy flux incident on the ionosphere, and the height-integrated Pedersen conductivity, respectively. The dashed-dotted line is the solution to the $\Phi_{||}$ = 0 approximation for comparison.

The field-aligned potential and incident energy flux profiles turnover ~33 R_J. The field-aligned current density does not decrease immediately with the change in $d\Phi_{||}/dr$ due to the saturation of $J_{||}^I$.

[50] The trend for the angular velocity profile follows that of the **I** × **B** force with the angular velocity profile remaining closer to rigid corotation out to larger equatorial radii for smaller R_x. The large **I** × **B** force for the R_x = 11 case accelerates the magnetospheric plasma in the corotational direction. For R_x = 11, the plasma angular velocity becomes supercorotational in the middle magnetosphere. This is not a physical solution.

[51] The auroral emission width and brightness vary greatly between the case of R_x = 11 and the cases of R_x = 16, 21, and 27. For the latter three cases, the width of the auroral emission is nearly constant at ~0.7° at Jupiter's atmosphere and maps to the same equatorial location of ~28 R_J. The energy flux incident on the ionosphere, and hence auroral brightness decreases slightly with increases in R_x. For R_x = 11, the energy flux incident on the ionosphere is over three times greater than in the other cases, peaking at ~30 mW/m^2. The intense aurora is due to the low-altitude location of the auroral acceleration region. The saturated field-aligned current density allows larger field-aligned potentials, increasing the incident energy flux. The width of the auroral oval is also increased for the lower R_x, mapping to an ionospheric width of ~1° and an equatorial mapping location of ~33 R_J. The Pedersen conductivity feedback, which is related to the energy flux incident on the ionosphere and the electron precipitation energy, follows the same trend with the strongest feedback occurring for R_x = 11. The dip in the Σ_P profile for R_x = 11 occurs when the electron precipitation energy is greater than 80 keV. These high-energy electrons precipitate through the peak Pedersen conducting layer, limiting the enhancement of the Pedersen conductance.

5. Discussion

[52] Our model extends previous work to self-consistently include field-aligned potentials, and their subsequent affect on the height-integrated Pedersen conductivity while evaluating the current system associated with Jupiter's main auroral emission. The auroral current system can be described as two coupled differential equations which require three boundary conditions; ω_0, $\Phi_{||0}$, and $\left(\frac{d\Phi_{||}}{dr}\right)_0$. We solve the system of equations using two independently developed numerical techniques. The solutions from the more accurate CPC technique agree with those from the more approximate CCT.

[53] We find a set of solutions, depending on the choice $\left(\frac{d\Phi_{||}}{dr}\right)_0$, which describe the auroral current system. An outer constraint is employed to determine $\left(\frac{d\Phi_{||}}{dr}\right)_0$. This outer constraint can be the total radial current at 100 R_J, the maximum field-aligned potential, or the maximum energy flux. We choose either I_{100} = 86 MA or $\Phi_{||Max}$ = 75 kV for the purpose of this study. These constraints are consistent with Galileo measurements and HST observations, respectively. For an $\dot{M}$ = 500 kg/s and an I_{100} = 86 MA the modeled auroral oval has a peak energy flux of 23 mW/m^2 and a peak precipitation electron energy of ~115 keV, consistent with parameters derived from HST observations. The auroral emission maps to ~40 R_J.

Table 4. Variation in Modeled Auroral Parameters with Location of the Acceleration Region (R_x) for I_{100} = 86 MA, Σ_{P_0} = 0.1 mho, ε = 1.0, T_e = 2.5 keV, n_0 = 0.01 cc^{-1}

R_x	Max. EF (mW/m^2)	Max. $\Phi_{||}$ (kV)	Equation Location (R_J)	Max. Ω/Ω_J (%)
11	30.9	209.5	33.4	103.7
16	10.0	58.2	28.2	95.1
21	7.9	45.5	28.2	94.9
27	7.0	40.1	28.4	94.9

[54] We assume a steady state auroral current system and spin-aligned dipole consistent with past models [e.g., *Hill*, 1979; *Pontius*, 1997; *Cowley and Bunce*, 2001; *Nichols and Cowley*, 2004]. Jupiter's main auroral emission is nearly constant in System III, however variation has been observed with interplanetary solar wind conditions as well as often observed brightenings in the dawn sector [*Clarke et al.*, 2004; *Gustin et al.*, 2006; *Nichols et al.*, 2007; *Clarke et al.*, 2009; *Nichols et al.*, 2009]. The inclusion of time dependence in the model would affect the electric field mapping between the ionosphere and the magnetosphere as the time variability of the magnetic field would enter into equation (17). Given the simplicity of our 1-D model, the assumption of a spin-aligned dipole is reasonable for this analysis. The fields and currents are mapped from the atmosphere to the magnetosphere using conservation of magnetic flux, which is derived using distances from the magnetic axis and coincident with the spin axis for our analysis. However, in the case of a tilted magnetic field, the relevant distances to map fields and currents would still be measured from the magnetic axis and therefore we would not expect a significant change in the solutions.

[55] Currently, the outer boundary of the equatorial mapping location for the main auroral emission is constrained by corotational features in the main auroral oval. The poleward boundary of the auroral emission is predicted to map inside ~30 R_J based on HST observations [*Clarke et al.*, 2004]. As this study has shown, field-aligned potentials decouple the rotation of Jupiter from that of its magnetosphere and increase the $\mathbf{I} \times \mathbf{B}$ force in the equatorial plane. The magnetospheric plasma remains near rigid corotation out to larger equatorial distances than shown in previous models [*Hill*, 1979; *Nichols and Cowley*, 2004] for realistic radial mass transport rates and modest values of the Pedersen conductivity. As the magnetospheric plasma angular velocity remains near rigid corotation out to ~35 R_J for $\dot{M}$ = 1000 kg/s (section 4.2) and ~45 R_J for $\dot{M}$ = 500 kg/s (section 4.3), we propose that the main auroral emission may map to larger equatorial distances than previously suggested. *Grodent et al.* [2008] showed that Ganymede's auroral footprint is occasionally observed in the main auroral emission, marking clearly the innermost equatorial mapping location of the emission at $r \sim 15R_J$. *Grodent et al.* [2008] also observed that the latitude of the main auroral emission can shift by ~3°. This slight shift at the atmosphere corresponds to a large shift in the magnetosphere due to the highly distended magnetic field (Figure 2). However, preliminary results indicate that the main auroral emission for a radial mass transport rate of 500 kg/s would be mapped to smaller equatorial radii when the input parameters are varied, e.g., n_0 is decreased. The mapping location of the auroral emission is also very dependent on the magnetic field model used.

[56] All models to date are limited to an axially symmetric magnetosphere from 5 to 100 R_J. However, the jovian magnetosphere displays local time variations outside ~20 R_J [*Krupp et al.*, 2001], with even stronger variation outside 40 R_J. The local time variations are driven by the solar wind interaction with the magnetosphere [*Hill et al.*, 1983; *Khurana et al.*, 2004; *Krupp et al.*, 2004; *Delamere and Bagenal*, 2010]. The local time variations in the magnetic field are pronounced, with a narrow current sheet and stretched magnetic field configuration in the dawn sector and a wide current sheet and hence more dipolar magnetic field configuration in the dusk sector [*Khurana*, 2001]. The azimuthal velocity of the magnetospheric plasma is greater in the predawn through prenoon sector than in the dusk through midnight sectors [*Krupp et al.*, 2001]. As the auroral current system is driven by deviations in the azimuthal velocity of the magnetospheric plasma from corotation, it is reasonable to suggest that the mapping location of the auroral emission may vary with local time, corresponding to the measured flows. An interesting extension of this study would be to investigate the changes in the auroral current system by modifying the magnetic field model to represent different local time sectors.

[57] There is a range of estimates of the background ionospheric Pedersen conductance at Jupiter based on previous modeling efforts of the magnetosphere-ionosphere coupling system [*Dessler and Hill*, 1979; *Hill*, 1980; *Vasyliunas*, 1983; *Nichols and Cowley*, 2004]. We choose Σ_{P_0} = 0.1 mho in the current study to be consistent with past work. However, the background conductance likely varies with local time and due to solar energy inputs is expected to be greater on the dayside than on the nightside. The variation in Σ_{P_0} may alter the mapping location of the main auroral oval with local time and would be an interesting study for future work.

[58] Our model predicts incident energy fluxes which are consistent with the ~2 to ~30 mW/m^2 derived by *Gustin et al.* [2004]. *Gustin et al.* [2004] analyzes 23 STIS spectra taken over a period of time from July 1997 through January 2001 to determine the mean incident energy flux, thus reflecting the average conditions of the main auroral emission. *Gustin et al.* [2006] investigates the auroral energy inputs associated with bright dawn auroral arcs, deriving the mean electron energies and incident energy fluxes for four bright regions of a dawn auroral arc. The analysis finds a maximum energy flux of ~110 mW/m^2, nearly four times greater than the mean incident energy flux found by *Gustin et al.* [2004]. Modeling bright auroral arcs is a future task for this model, however preliminary results indicate that the incident energy flux can be increased by decreasing the mass transport rate, increasing the electron density in the auroral cavity, or decreasing the energy of the auroral electrons, as well as moving the auroral acceleration region toward Jupiter as described in section 4.5 for a fixed outer constraint of I_{100} = 86 MA.

[59] Another limitation of our model is the assumption of a purely upward current system. Field-aligned currents transfer angular momentum to Jupiter's magnetosphere from 5 to 100 R_J, with no return current. As discussed in section 1, the location of the downward current is not well known. The interspersing of upward and downward current regions would substantially change the auroral current structure. However, there must be a net upward current in the middle magnetosphere which transfers angular momentum out from Jupiter to the equatorial plasma. Including the downward current system in our model would likely move the auroral mapping location in toward Jupiter and yield a more symmetric field-aligned potential profile as the downward current region demands that the field-aligned potentials return to zero.

[60] As the entire current circuit is not included in our model, we do not include an energy equation and therefore

must set an outer boundary constraint to select our solution. A global energy equation for the system is a necessary next step in constraining the auroral currents system. However, the jovian magnetosphere is a dynamic system which "chooses" a solution to the auroral currents while accounting for energy conservation, local time variations, time variability, and plasma production rates as the system evolves.

[61] The JUNO spacecraft, which arrives at Jupiter in 2016, will intersect auroral flux tubes at high latitudes. JUNO will likely fly through the region of field-aligned potentials making in situ measurements of particles and fields. These measurements can then be used to determine the field-aligned currents and field-aligned potentials in the auroral region, testing our ideas of the jovian auroral current system. JUNO's polar orbit will help determine the higher-order moments of the jovian magnetic field, improving the magnetic field models and the precision in the mapping of the auroral region out to the magnetosphere.

6. Conclusion

[62] We find that including field-aligned potentials in the current system driving Jupiter's main auroral emission modifies the system behavior, allowing differential rotation between the magnetosphere from the ionosphere and increasing the field-aligned currents which transfer angular momentum from the planet to the magnetospheric plasma. We describe the current system causing Jupiter's main auroral emission as two coupled differential equations requiring three boundary conditions; ω_0, $\Phi_{\|_0}$, and $\left(\frac{d\Phi_\|}{dr}\right)_0$. We draw the following conclusions:

[63] 1. We find a set of solutions depending on the boundary condition $\left(\frac{d\Phi_\|}{dr}\right)_0$ which is determined by setting an outer constraint of either the total radial current at 100 R_J or the maximum field-aligned potential.

[64] 2. Our solutions reproduce the main features of the aurora: (a) the observed width of the main auroral oval (~1° at Jupiter); (b) the equatorial mapping location of the auroral emission (20–30 R_J); and (c) auroral electron precipitation energies (50–125 keV) and incident energy fluxes (10–25 mW/m^2 consistent with those derived from HST-STIS observations (30–200 keV and 2–30 mW/m^2, respectively, for a radial mass transport rate of 1000 kg/s).

[65] 3. Our model produces the large radial currents (86 MA) derived by Galileo data with a more realistic radial mass transport rate ($\dot{M}$ ~ 500 kg/s) which is significantly smaller than previous models and consistent with the $\dot{M}$ determined by modeling the Io torus UV emission observed by Cassini. This lower $\dot{M}$ value pushes the auroral mapping region out to ~40 R_J.

[66] 4. The inclusion of field-aligned potentials increases the field-aligned current density by (a) boosting the electron distribution function into the loss cone and (b) increasing the electron precipitation energy and incident energy flux at the ionosphere, which enhances the Pedersen conductivity. The sharp increase in field-aligned currents with radial distance from ~15 to ~20 R_J increases the $\mathbf{I} \times \mathbf{B}$ force in the magnetosphere.

[67] 5. The field-aligned potentials are a significant fraction of the rotational potential in the middle magnetosphere and therefore cannot be neglected when mapping electric fields.

[68] 6. The relative roles of field-aligned potentials and the Pedersen conductivity vary with the location of the acceleration region (R_x). For small R_x, the current density grows steeply over a short radial distance and then saturates. The field-aligned potentials allow for a significant difference in the rotation of the magnetosphere from that of the ionosphere, driving large Pedersen conductivities and a bright auroral emission. For larger R_x the interplay between the Pedersen conductivity and the field-aligned potentials is more subtle. The Pedersen conductivity contributes more strongly to the increase in the field-aligned current density, and the growth of the field-aligned potential is limited, resulting in a dimmer auroral emission.

Appendix A: Pedersen Conductivity

[69] Variations in the energy of precipitating electrons at the ionosphere and the incident energy flux modify the height-integrated ionospheric Pedersen conductivity. The Pedersen conductivity increases with incident energy flux. It also increases with the energy of the precipitating electrons, however when the electrons are energetic enough to precipitate below the peak conducting layer, i.e., where the ion gyrofrequency equals the ion-neutral collision frequency, the Pedersen conductivity begins to decrease with increasing precipitation energy. *Millward et al.* [2002] found that the Pedersen conductivity maximizes for a precipitation energy of ~60 keV. *Millward et al.* [2002] described the variation in Pedersen conductivity with energy flux for a constant electron precipitation energy and the variation with precipitating electron energy for a constant energy flux. They did not determine a function for the Pedersen conductivity which varies with both parameters. In addition, the electron precipitation energy in their analysis referred to the energy derived from the parallel component of the electron velocity.

[70] In order to find a function for the Pedersen conductivity which depends on the energy of the precipitating electrons and the incident energy flux we must first select an electron distribution function which describes the auroral population. We use a shell distribution for the electrons which is consistent with measurements of auroral electron populations from the FAST satellite at Earth [*Ergun et al.*, 2000]. The electron energy is nearly constant in a shell distribution, however the parallel electron energy varies with pitch angle. We assume that the parallel electron energy is the energy that an electron would gain from acceleration through the field-aligned potential for this analysis.

[71] The parallel energy flux ($EF(\varepsilon_\|)$) for a given electron distribution is

$$EF(\varepsilon_\|) = \sum f(v) v_\| e\Phi d^3 v \tag{A1}$$

For a shell distribution, this is

$$EF(\varepsilon_\|) = \sum_{v_\|=0}^{v_0} f_0 2\pi v_\perp v_\| v_\perp v_\| (e\Phi_0) \tag{A2}$$

where $f_0 = n_0/(2\pi v_0^2\ \Delta v)$ is the electron distribution function of the shell. Removing the dependence on the perpen-

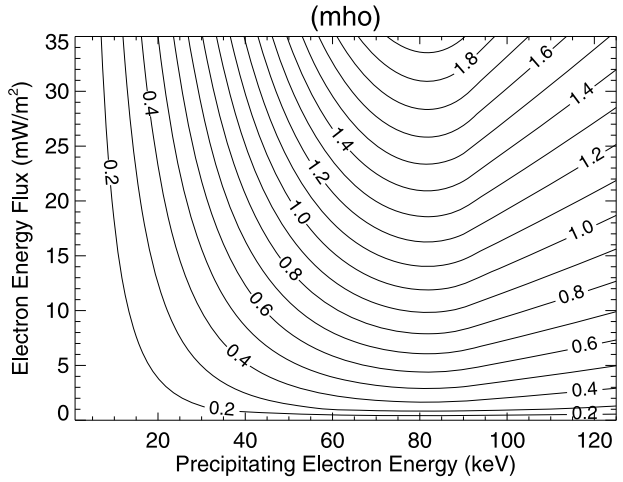

Figure A1. Pedersen conductivity profile as a function of electron precipitation energy and incident energy flux. The modified function is based off of results from *Millward et al.* [2002]. The Pedersen conductivity peaks for an electron precipitation energy of ~80 keV.

dicular velocity, we find that the electron energy flux can be expressed as a function of $v_\parallel$:

$$EF(\varepsilon_\parallel) = \sum_{v_\parallel=0}^{v_0} 2\pi f_0 v_0 \Delta v \Delta v_\parallel v_\parallel e\Phi_0 \tag{A3}$$

The partial energy flux at each parallel energy is then described as:

$$\delta EF = \frac{EF(\varepsilon_\parallel)}{\Delta\varepsilon_\parallel} = \frac{n_0 v_0 \Delta\varepsilon}{2} \tag{A4}$$

With the above expression we can convolve the Pedersen conductivity as a function of precipitating electron energy from Figure 8b of *Millward et al.* [2002], for a fixed energy flux of 10 mW/m^2, with the energy flux for a shell distribution of auroral electrons (equation (A4)). The adjusted Pedersen conductivity as a function of field-aligned potential is fit by

$$\Sigma_{P_{\Phi_\parallel \le 93keV}}(\Phi_\parallel) = A_1\Phi_\parallel + A_2\Phi_\parallel^2 + A_3\Phi_\parallel^3 \tag{A5}$$

where $A_1 = 4.58164 \times 10^{-6}$, $A_2 = 2.49649 \times 10^{-10}$ and $A_3 = -2.26522 \times 10^{-15}$ for precipitating electron energies up to 93 keV. As the *Millward et al.* [2002] analysis only explores the variation in Pedersen conductance for precipitating electron energies less than 100 keV, we use an exponential decrease with $\Phi_\parallel$ for precipitating electron energies greater than 93 keV:

$$\Sigma_{P_{\Phi_\parallel > 93keV}}(\Phi_\parallel) = \Sigma_{P_{\Phi_\parallel \le 93keV}}(93keV)\frac{e^{-(\Phi_\parallel/1keV)^{1/4}}}{e^{-(93keV/1keV)^{1/4}}} \tag{A6}$$

The variation in Pedersen conductivity with incident energy flux from *Millward et al.* [2002, equation (3)] is

$$\Sigma_{P_{EF}}(EF) = (EF^{\alpha_P}10^{\gamma_P})10^{\beta_P(\log_{10}E_f)^2} \tag{A7}$$

[72] We then convolve equations (A5) and (A7) to obtain our new Pedersen conductivity function which varies with electron precipitation energy and incident electron energy flux

$$\Sigma_P(\Phi, EF) = \Sigma_{P_0} + e\frac{\Sigma_{P_{\Phi_\parallel}}(\Phi_\parallel)\Sigma_{P_{EF}}(EF)}{\Sigma_{P_{EF}}(10mW/m^2)} \tag{A8}$$

where we have normalized the above expression to an energy flux of 10 mW/m^2 so that it matches the results of *Millward et al.* [2002]. The factor of ε is present to modify the efficiency of the Pedersen conductivity enhancement. This factor is equal to unity except to explore the interplay between the field-aligned potentials and the Pedersen conductivity. The Pedersen conductivity expressed in equation (A8), with $\varepsilon = 1$, is plotted in Figure A1. The main difference between the Pedersen conductivity given by *Millward et al.* [2002] and equation (A8) is that our function peaks at a precipitation energy of ~80 keV, which is 20 keV more than peak conductivity from the *Millward et al.* [2002] function. In addition, the maximum Pedersen conductivity is decreased by ~0.2 mho as variations in the Pedersen conductivity with electron precipitation energy, as modified by equation (A4) due to a spherical shell distribution of auroral electrons, are spread over a broader range of precipitation energies.

Appendix B: Numerical Solutions

[73] The numerical solutions are found using two different techniques. Both techniques start with a set of boundary conditions at ~6 R_J. The two techniques use identical magnetic field mappings and identical Pedersen conductivity functions, but have a small difference in the current-voltage relation that is described below. Since the governing equations are higher order, an additional constraint must be introduced to get unique solutions.

[74] The two techniques introduce this additional constraint with different methods. The first technique, called a "critical current technique" (CCT), solves the linear approximation ($E_M = E_I$) from 6 R_J to r_{crit} with a simple differential method. The linear solver is valid as long as the current-voltage relation has a relatively high effective conductivity, $d\Phi_\parallel/dJ_\parallel^I \sim 0$. Once a critical current is reached, $J_\parallel^I \ge J_{crit.}$, the solution is stopped. At the location of the critical current, r_{crit}, the additional boundary condition is introduced by applying a small gradient in the potential, $d\Phi_\parallel/dr$. The CCT then applies the integral operators (Table B1) to continue with the solution. The integral operators are stable as long as the current-voltage relation is above a threshold resistance, that is $d\Phi_\parallel/dJ_\parallel^I > \varepsilon$ (see later). Since the quantity $d\Phi_\parallel/dr$ has not been

Table B1. Numerical Integrator

Step	Equation	Comment
1	$\frac{d\omega}{dr} = \frac{2\pi K_m B_m}{M} - \frac{2(\Omega_J+\omega)}{r}$	High-order integrator
2	$E_M = \omega\ rB_M$	Multiply
3	$\frac{dK_M}{dr} = -\frac{K_M}{r} + 2J_\parallel^M$	High-order integrator
4	$E_I^* = -\frac{1}{2}K_M\Sigma_P\frac{r}{\alpha s}$	Multiply
5	$\frac{d\Phi_\parallel}{dr} = E_M - E_I^*$	Integrator
6	$J_\parallel^M = \frac{1}{R_M}J_\parallel^I(\Phi_\parallel)$	Function

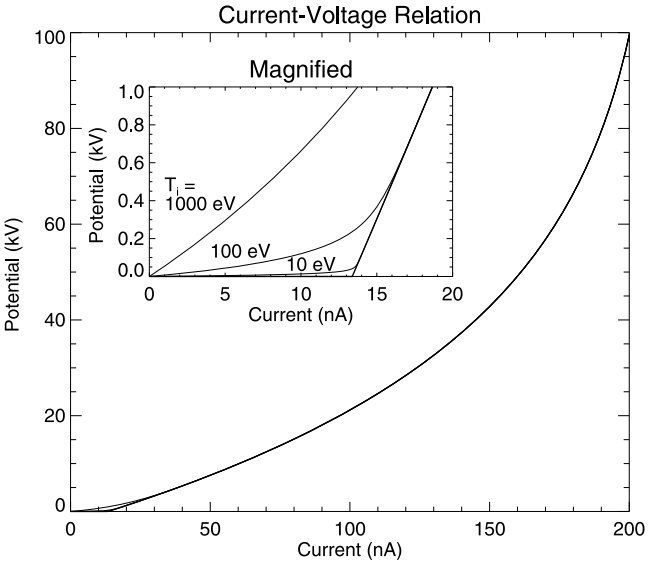

Figure B1. The current-voltage relation plotted for several temperatures (T_i) with $j_i - j_x$. The thick line is equation (19), and the thin line is from equation (B3).

measured, its value is varied to obtain a set of solutions such as presented in Figure 3.

[75] Applying the boundary condition at Io's orbit rather than at r_{crit} would be much more satisfying. The difficulty is best discussed by linearizing the equations (Table B1) and examining the behavior of the system over a short distance in E_Mr or E_Ms. The deviation from corotation (ω) and radial current (K_M) slowly varies with E_Mr and E_Ms. Physically, one can envision that a large change in rotation rate of the plasma over a short radial distance would require very large radial current and an even larger change in the radial current. Such a large change in the radial current over a short distance would require unrealistically large field-aligned currents. As a consequence, ω, K_M, and E_M slowly vary with radial distance.

[76] The local solution will: (1) assume E_M is zero (or constant); (2) linearize the current voltage relation by introducing a conductivity, $J_\parallel = \sigma_\parallel \Phi_\parallel$; (3) approximate the current conductivity as $J_\parallel(s) - dK_I/ds$; and, for simplicity, (4) will be solved in the ionosphere. The governing equations reduce to [*Lyons*, 1980; *Ergun et al.*, 2009]:

$$\frac{d^2\Phi_\parallel}{ds^2} = \sigma_\parallel 2\Sigma_P \Phi_\parallel \tag{B1}$$

which has the solution

$$\Phi_\parallel(s) = \Phi_{\parallel_0} e^{\pm s/s_0}, s_0 = \sqrt{2\Sigma_P/\sigma_\parallel} \tag{B2}$$

The scale size (s_0) depends on the ratio of the Pedersen conductivity (Σ_P) to the parallel conductivity ($\sigma_\parallel$). Current-voltage relation has high conductivity if $J_\parallel^I < J_{crit}$ [*Ray et al.*, 2009] for 6 $R_J \le r < r_{crit.}$, so the scale size is very small; as $\sigma_\parallel \to \infty$, $s_0 \to 0$. At these radial distances, the exponential growth of a small numerical error in $\Phi_\parallel$ will dominate the solution of the nonlinear equations. In other words, numerical integration from the Io boundary can be unstable.

[77] A second, independent numerical method was employed to verify the critical current technique. This technique, called a "constrained predictor-corrector" (CPC), basically searches for solutions by controlling the accumulated error in the potential from 6 $R_J \le r \lesssim 12$ R_J. The additional constraint can be one of the value of the maximum potential ($\Phi_{\parallel \mathrm{Max}}$) in the simulation domain 6 $R_J \le r \le 100$ R_J or the total radial current (I_{100}) at E_Mr = 100 R_J. The code advances in E_Mr from E_Mr = 6 R_J by "looking ahead." At each step, the code integrates to a full solution over the simulation domain then applies a correction to $\Phi_\parallel$ (or ω) at the level of 10^{-15} (double precision). In other words, it controls the rounding of the least significant bits of a double-precision number so an error in $\Phi_\parallel$

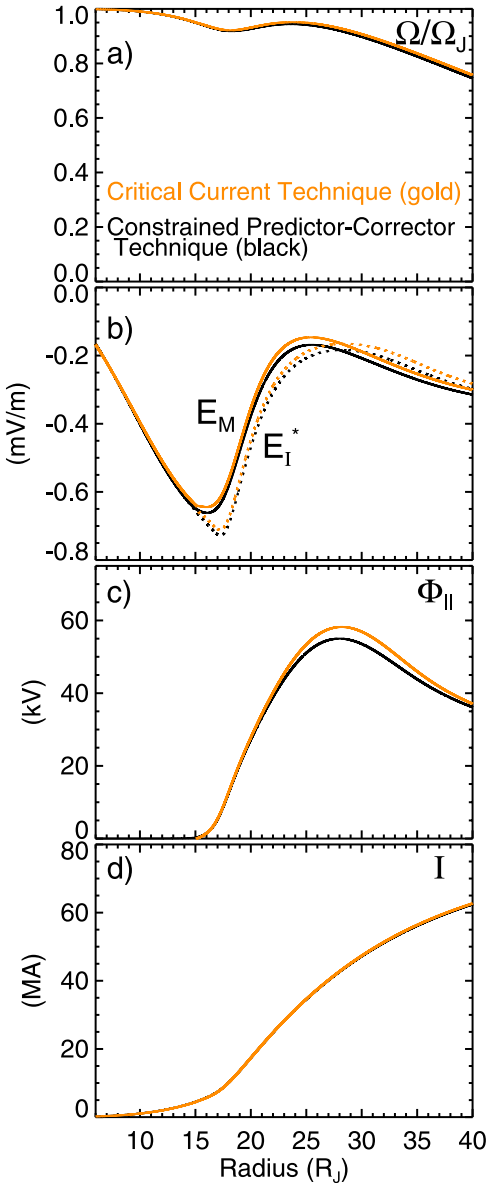

Figure B2. (a) The deviation from rotation, (b) the ionospheric (dashed-dotted lines) and magnetospheric (solid lines) electric fields, (c) the field-aligned potentials, and (d) the radial currents from the "critical current technique" (gold lines) and the "constrained predictor-corrector" technique (black lines).

does not accumulate. The correction is applied at each step in E_Mr until the constraint (designated $\Phi_{\|\mathrm{Max}}$ or designated I_{100}) is met. Typically, no corrections are needed after E_Mr ~ 12 R_J. The CPC simultaneously keeps the solutions accurate to levels achievable by double-precision and introduces the additional constraint. To achieve the needed accuracy, the CPC requires small integration steps (a large number of positions, N) and must perform $O(N^2)$ calculations, so it is far more computationally demanding that the critical current technique. Results from the CCT are verified by the CPC.

[78] The CPC requires a finite conductivity at all locations in E_Mr (Table B1, step 6), so a more exact current-voltage relation is adopted rather than using the approximation (equation (19)). Here we use the form

$$J_{\|}^{I} = J_{\|}^{M} R_M = j_x + j_x(R_x - 1)\left(1 - e^{-\left(\frac{e\Phi_{\|}}{T_x(R_x-1)}\right)}\right) - j_1 e^{-\frac{e\Phi_{\|}}{T_e^{Iono.}}} \quad \text{(B3)}$$

The equation is identical to that in equation (19) except for the last term [*Boström*, 2003], which represents the thermal electron current from the Ionosphere (j_i). The current is controlled by the temperature of this electron population ($T_e^{Iono.}$). It is typically omitted from analysis since often $T_e^{Iono} \ll T_x$. Inclusion of this term allows us to use a continuous current-voltage relation (Figure B1) that is otherwise identical to that expressed in equation (19).

[79] Figure B2 displays a comparison between the critical current technique and the constrained predictor-corrector ($T_e^{Iono.}$ = 100 eV) of the solution described in section 4.2. The deviations from corotation (Figure B2a) agree well. Both solutions were constrained to I_{100} = 86 MA, so the radial currents (Figure B2d) naturally agree well. The small differences in the electric fields (Figure B2b) and the net field-aligned potentials (Figure B2c) are consistent with the differences in the current-voltage relation. We conclude that the small error introduced in the critical current technique does not substantially alter the solutions.

[80] **Acknowledgments.** The authors wish to thank John Clarke, Chris Cully, Vincent Dols, Jonny Nichols, Yi-Jiun Su, Stan Cowley, and Frank Crary for helpful conversations. The work was partially supported by NASA's JUNO mission and NESSF program.

[81] Bob Lysak thanks the reviewers for their assistance in evaluating this paper.

References

Belcher, J. W. (1983), The low-energy plasma in the Jovian magnetosphere, in *Physics of the Jovian Magnetosphere*, edited by A. J. Dessler, pp. 68–105, Cambridge Univ. Press, New York.

Bonfond, B., D. Grodent, J. Gérard, A. Radioti, V. Dols, P. A. Delamere, and J. T. Clarke (2009), The Io UV footprint: Location, interspot distances and tail vertical extent, *J. Geophys. Res.*, *114*, A07224, doi:10.1029/2009JA014312.

Boström, R. (2003), Kinetic and space charge control of current flow and voltage drops along magnetic flux tubes: Kinetic effects, *J. Geophys. Res.*, *108*(A4), 8004, doi:10.1029/2002JA009295.

Clarke, J. T., D. Grodent, S. W. H. Cowley, E. J. Bunce, P. Zarka, J. E. P. Connerney, and T. Satoh (2004), Jupiter's aurora, in *Jupiter. The Planet, Satellites and Magnetosphere*, edited by F. Bagenal, T. E. Dowling, and W. B. McKinnon, pp. 639–670, Cambridge Univ. Press, New York.

Clarke, J. T., et al. (2009), Response of Jupiter's and Saturn's auroral activity to the solar wind, *J. Geophys. Res.*, *114*, A05210, doi:10.1029/2008JA013694.

Connerney, J. E. P., M. H. Acuna, and N. F. Ness (1981), Modeling the Jovian current sheet and inner magnetosphere, *J. Geophys. Res.*, *86*(A10), 8370–8384, doi:10.1029/JA086iA10p08370.

Cowley, S. W. H., and E. J. Bunce (2001), Origin of the main auroral oval in Jupiter's coupled magnetosphere-ionosphere system, *Planet. Space Sci.*, *49*, 1067–1088.

Delamere, P. A., and F. Bagenal (2010), Solar wind interaction with Jupiter's Magnetosphere, *J. Geophys. Res.*, doi:10.1029/2010JA015347, in press.

Delamere, P. A., F. Bagenal, and A. Steffl (2005), Radial variations in the Io plasma torus during the Cassini era, *J. Geophys. Res.*, *110*, 12,223–12,236, A12223, doi:10.1029/2005JA011251.

Dessler, A. J., and T. W. Hill (1979), Jovian longitudinal control of Io-related radio emissions, *Astrophys. J.*, *538*, 664–675.

Ergun, R. E., C. W. Carlson, J. P. McFadden, G. T. Delory, R. J. Strangeway, and P. L. Pritchett (2000), Electron-cyclotron maser driven by charged-particle acceleration from magnetic field-aligned electric fields, *Astrophys. J.*, *538*, 456–466.

Ergun, R. E., L. Ray, P. A. Delamere, F. Bagenal, V. Dols, and Y. Su (2009), Generation of parallel electric fields in the Jupiter-Io torus wake region, *J. Geophys. Res.*, *114*, A05201, doi:10.1029/2008JA013968.

Frank, L. A., and W. R. Paterson (2002), Galileo observations of electron beams and thermal ions in Jupiter's magnetosphere and their relationship to the auroras, *J. Geophys. Res.*, *107*(A12), 1478, doi:10.1029/2001JA009150.

Grodent, D., J. Gérard, A. Radioti, B. Bonfond, and A. Saglam (2008), Jupiter's changing auroral location, *J. Geophys. Res.*, *113*, A01206, doi:10.1029/2007JA012601.

Gustin, J., J. -C. Gérard, D. Grodent, S. W. H. Cowley, J. T. Clarke, and A. Grard (2004), Energy-flux relationship in the FUV Jovian aurora deduced from HST-STIS spectral observations, *J. Geophys. Res.*, *109*, A10205, doi:10.1029/2003JA010365.

Gustin, J., S. W. H. Cowley, J. -C. Gérard, G. R. Gladstone, D. Grodent, and J. T. Clarke (2006), Characteristics of Jovian morning bright FUV aurora from Hubble Space Telescope/Space Telescope Imaging Spectrograph imaging and spectral observations, *J. Geophys. Res.*, *111*, A09220, doi:10.1029/2006JA011730.

Hill, T. W. (1979), Inertial limit on corotation, *J. Geophys. Res.*, *84*, 6554–6558, doi:10.1029/JA084iA11p06554.

Hill, T. W. (1980), Corotation lag in Jupiter's magnetosphere—Comparison of observation and theory, *Science*, *207*, 301–302.

Hill, T. W., and V. M. Vasyliūnas (2002), Jovian auroral signature of Io's corotational wake, *J. Geophys. Res.*, *107*(A12), 1464, doi:10.1029/2002JA009514.

Hill, T. W., A. J. Dessler, and F. C. Michel (1974), Configuration of the Jovian atmosphere, *Geophys. Res. Lett.*, *1*(1), 3–6, doi:10.1029/GL001i001p00003.

Hill, T. W., A. J. Dessler, and C. K. Goertz (1983), Magnetospheric models, in *Physics of the Jovian Magnetosphere*, edited by A. J. Dessler, pp. 353–394, Cambridge Univ. Press, New York.

Khurana, K. K. (2001), Influence of solar wind on Jupiter's magnetosphere deduced from currents in the equatorial plane, *J. Geophys. Res.*, *106*(A11), 25,999–26,016, doi:10.1029/2000JA000352.

Khurana, K. K., and M. G. Kivelson (1993), Inference of the angular velocity of plasma in the Jovian magnetosphere from the sweepback of magnetic field, *J. Geophys. Res.*, *98*(A1), 67–79, doi:10.1029/92JA01890.

Khurana, K. K., M. G. Kivelson, V. M. Vasyliunas, N. Krupp, J. Woch, A. Lagg, B. H. Mauk, and W. S. Kurth (2004), The configuration of Jupiter's magnetosphere, in *Jupiter. The Planet, Satellites and Magnetosphere*, edited by F. Bagenal, T. E. Dowling, and W. B. McKinnon, pp. 593–616, Cambridge Univ. Press, New York.

Kivelson, M. G., K. K. Khurana, and R. J. Walker (2002), Sheared magnetic field structure in Jupiter's dusk magnetosphere: Implications for return currents, *J. Geophys. Res.*, *107*(A7), 1116, doi:10.1029/2001JA000251.

Knight, S. (1973), Parallel electric fields, *Planet. Space Sci.*, *21*, 741–750.

Krupp, N., et al. (2004), Dynamics of the Jovian magnetosphere, in *Jupiter. The Planet, Satellites and Magnetosphere*, edited by F. Bagenal, T. E. Dowling, and W. B. McKinnon, pp. 617–638, Cambridge Univ. Press, New York.

Krupp, N., A. Lagg, S. Livi, B. Wilken, J. Woch, E. C. Roelof, and D. J. Williams (2001), Global flows of energetic ions in Jupiter's equatorial plane: First-order approximation, *J. Geophys. Res.*, *106*(A11), 26,017–26,032, doi:10.1029/2000JA900138.

Lyons, L. R. (1980), Generation of large-scale regions of auroral currents, electric potentials, and precipitation by the divergence of the convection electric field, *J. Geophys. Res.*, *85*(A1), 17–24, doi:10.1029/JA085iA01p00017.

Mauk, B. H., and J. Saur (2007), Equatorial electron beams and auroral structuring at Jupiter, *J. Geophys. Res.*, *112*, A10221, doi:10.1029/2007JA012370.

Mauk, B. H., B. J. Anderson, and R. M. Thorne (2002), Magnetosphere-ionosphere coupling at Earth, Jupiter, and beyond, in *Atmospheres in the Solar System: Comparative Aeronomy*, *Geophys. Monogr. Ser.*, vol. 130, edited by M. Mendillo, A. Nagy, and J. H. Waite, pp. 97–114, AGU, Washington, D. C.

McNutt, R. L., Jr., J. W. Belcher, J. D. Sullivan, F. Bagenal, and H. S. Bridge (1979), Departure from rigid corotation of plasma in Jupiter's dayside magnetosphere, *Nature*, *280*, 803.

Melrose, D. B. (1967), Rotational effects on the distribution of thermal plasma in the magnetosphere of Jupiter, *Planet. Space Sci.*, *15*, 381–393.

Millward, G., S. Miller, T. Stallard, A. D. Aylward, and N. Achilleos (2002), On the dynamics of the Jovian ionosphere and thermosphere: III. The modelling of auroral conductivity, *Icarus*, *160*, 95–107.

Nichols, J., and S. Cowley (2004), Magnetosphere-ionosphere coupling currents in Jupiter's middle magnetosphere: Effect of precipitation-induced enhancement of the ionospheric Pedersen conductivity, *Ann. Geophys.*, *22*, 1799–1827.

Nichols, J. D., and S. W. H. Cowley (2005), Magnetosphere-ionosphere coupling currents in Jupiter's middle magnetosphere: Effect of magnetosphere-ionosphere decoupling by field-aligned auroral voltages, *Ann. Geophys.*, *23*, 799–808.

Nichols, J. D., E. J. Bunce, J. T. Clarke, S. W. H. Cowley, J. Gérard, D. Grodent, and W. R. Pryor (2007), Response of Jupiter's UV auroras to interplanetary conditions as observed by the hubble space telescope during the Cassini flyby campaign, *J. Geophys. Res.*, *112*, A02203, doi:10.1029/2006JA012005.

Nichols, J. D., J. T. Clarke, J. C. Gérard, D. Grodent, and K. C. Hansen (2009), Variation of different components of Jupiter's auroral emission, *J. Geophys. Res.*, *114*, A06210, doi:10.1029/2009JA014051.

Pontius, D. H. (1997), Radial mass transport and rotational dynamics, *J. Geophys. Res.*, *102*(A4), 7137–7150, doi:10.1029/97JA00289.

Pontius, D. H., Jr., and T. W. Hill (1982), Departure from corotation of the Io plasma torus—Local plasma production, *Geophys. Res. Lett.*, *9*(12), 1321–1324, doi:10.1029/GL009i012p01321.

Radioti, A., J. Gérard, D. Grodent, B. Bonfond, N. Krupp, and J. Woch (2008), Discontinuity in Jupiter's main auroral oval, *J. Geophys. Res.*, *113*, A01215, doi:10.1029/2007JA012610.

Ray, L. C., Y. Su, R. E. Ergun, P. A. Delamere, and F. Bagenal (2009), Current-voltage relation of a centrifugally confined plasma, *J. Geophys. Res.*, *114*, A04214, doi:10.1029/2008JA013969.

Scudder, J. D., E. C. Sittler, and H. S. Bridge (1981), A survey of the plasma electron environment of Jupiter—A view from Voyager, *J. Geophys. Res.*, *86*(A10), 8157–8179, doi:10.1029/JA086iA10p08157.

Su, Y., R. E. Ergun, F. Bagenal, and P. A. Delamere (2003), Io-related Jovian auroral arcs: Modeling parallel electric fields, *J. Geophys. Res.*, *108*(A2), 1094, doi:10.1029/2002JA009247.

Vasyliunas, V. M. (1983), Plasma distribution and flow, in *Physics of the Jovian Magnetosphere*, edited by A. J. Dessler, pp. 395–453, Cambridge Univ. Press, New York.

F. Bagenal, P. A. Delamere, R. E. Ergun, and L. C. Ray, Laboratory for Atmospheric and Space Physics, University of Colorado at Boulder, UCB392, Boulder, CO 80309-0392, USA. (licia.ray@colorado.edu)